J. Mech. Phys. Solids 188 (2024) 105630

Contents lists available at ScienceDirect

Journal of the Mechanics and Physics of Solids

journal homepage: www.elsevier.com/locate/jmps

Kresling origami mechanics explained: Experiments and theory

Shixi Zang [a], Diego Misseroni [b,*], Tuo Zhao [a], Glaucio H. Paulino [a,c,**]

[a] *Department of Civil and Environmental Engineering, Princeton University, Princeton, NJ, 08544, USA*
[b] *Department of Civil, Environmental and Mechanical Engineering, University of Trento, Italy*
[c] *Princeton Materials Institute (PMI), Princeton University, Princeton, NJ 085444, USA*

ARTICLE INFO

Keywords:
Origami
Kresling pattern
Potential energy

ABSTRACT

From a kinematics perspective, a Kresling origami cell couples axial displacement (contraction/expansion) with twist, leading to non-rigid origami behavior. From an energy landscape perspective, the selection of the Kresling origami geometry, together with its fabrication process and material, lead to energy envelopes allowing single or multiple stable states. In this context, this paper explores the Kresling origami mechanics through mathematical modeling integrated with experimental testing. On the theoretical mechanics front, we present a comprehensive model incorporating the representative geometrical parameters of the Kresling origami cell into the corresponding energy function in order to capture its essential mechanical behavior. On the experimental mechanics front, we create two fixtures that demonstrate the ability to control axial displacement (contraction/expansion) and twist independently, without imposing any constraints on the chiral arrangement of individual cells within the Kresling origami array (composed of multiple cells). Finally, we show the coexistence of multiple mechanical and morphological configurations within the same Kresling array by programming its loading modes, i.e., compression or twist. The fundamental nature of this work makes it applicable to several fields of engineering, including soft robotics and mechanical computing.

1. Introduction

We present a comprehensive theoretical analysis of the Kresling (2008) origami, incorporating its representative geometric parameters into the energy expression, thereby shedding light on how they influence the multistability behavior of the origami assembly. In addition, we introduce two novel experimental fixtures tailored for conducting either applied twist with free axial displacement or applied axial displacement with free twist. The uniqueness of the experimental apparatus lies in its ability to independently control axial displacement (contraction/expansion) and torsional motion. This feature allows testing of Kresling arrays consisting of either odd or even number of cells, without imposing constraints on the chiral arrangement of individual cells within the array, as illustrated by Fig. 1. By exploring local actuation of the Kresling array, we show coexistence of multiple mechanical and morphological configurations.

The remainder of this paper is organized as follows. In Section 2, we provide the motivation behind this paper by summarizing related work in both theory and experiments. Section 3 formulates the mechanics problem, considering geometry, mechanical properties, and their respective roles in the mechanical behavior of Kresling origami via parametric analysis. Section 4 describes the manufacturing method adopted to create the origami cells and provides a detailed description of the two experimental setups created for the experiments: the free-rotating fixture for compression experiments, and the free-translating fixture for torsional experiments. In Section 5, we discuss the results obtained with single Kresling cells and 2-cell Kresling arrays. Section 6 provides concluding

---

* Corresponding author.

** Corresponding author at: Department of Civil and Environmental Engineering, Princeton University, Princeton, NJ, 08544, USA.

E-mail addresses: diego.misseroni@unitn.it (D. Misseroni), gpaulino@princeton.edu (G.H. Paulino).

https://doi.org/10.1016/j.jmps.2024.105630
Received 26 January 2024; Received in revised form 23 March 2024; Accepted 25 March 2024

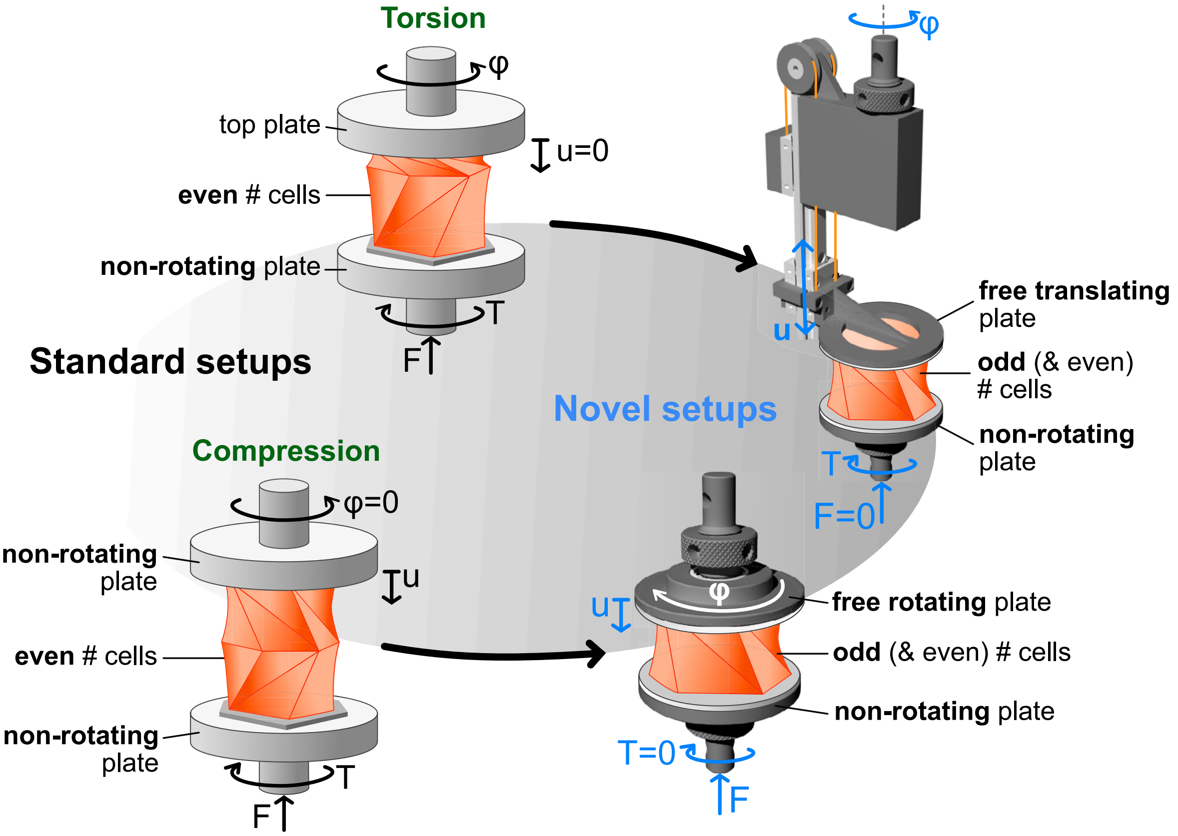

Fig. 1. Evolution of mechanical testing setups for Kresling origami cell coupling axial displacement (contraction/expansion) and twist. Top left: standard setup consisting of applied twist with prescribed axial displacement; Bottom left: standard setup consisting of applied axial displacement with prescribed twist; Top right: applied twist with free axial displacement; and Bottom right: applied axial displacement with free twist. Notice that the experimental setups (standard) on the left-hand-side are conducted with an even number of cells, while the experimental setups (novel) on the right-hand-side do not place any restriction on the number of cells, i.e. even or odd. The two novel experimental setups are explained later in the article.

remarks. Six Appendices supplement the paper. Appendix A presents further theoretical details about the formulation employed in this work, including the energy approach discussed in Section 3. Appendix B provides details of the Kresling cell fabrication. Appendix C investigates the effects of loading rate for the experimental setups. Appendix D reports auxiliary experiments conducted to estimate the mechanical properties of the composite material used for sample manufacturing and to estimate the rotational stiffness of the creases. Appendix E discusses the buckling effects observed in the torsional experiments of the 2-cell array with opposite chirality. Finally, Appendix F presents the nomenclature.

2. Motivation and scope of work

The findings of this study are applicable to several fields of engineering, including mechanical computing (Yasuda et al., 2021). They pave the way for the development of mechanical memory systems capable of encoding information. By exploring the sequence of mechanical loading (axial displacement or twist), we enable the coexistence of multiple mechanical/morphological states within the same structure, as illustrated by Fig. 2. Further exploration of this loading sequence-dependent phenomenon may lead to the creation of multifunctional structural and material systems with embedded mechanical computing systems.

2.1. Theoretical considerations

The theoretical analysis of Kresling origami structures is generally based on simplified models, as summarized by Fig. 3. For instance, one of those approaches considers a truss comprised of bar elements only. The stretching of the bar elements estimates the folding kinematics and predicts the mechanical behavior of the Kresling structure. The truss-based modeling assumes that the length of edges on the top and bottom polygons remains constant, while truss members along the mountain and valley creases deform during deployment. Cai et al. (2015) proposed a model considering that the lengths of mountain creases are constant while the length of valley creases can change. Conversely, Bhovad et al. (2019) assumed constant valley creases and variable mountain creases. However, these assumptions do not fully capture the folding behavior of the Kresling origami. Yasuda et al. (2017) built an elastic truss prototype and modeled mountain and valley creases as linear springs. This approach has been adopted by most of the

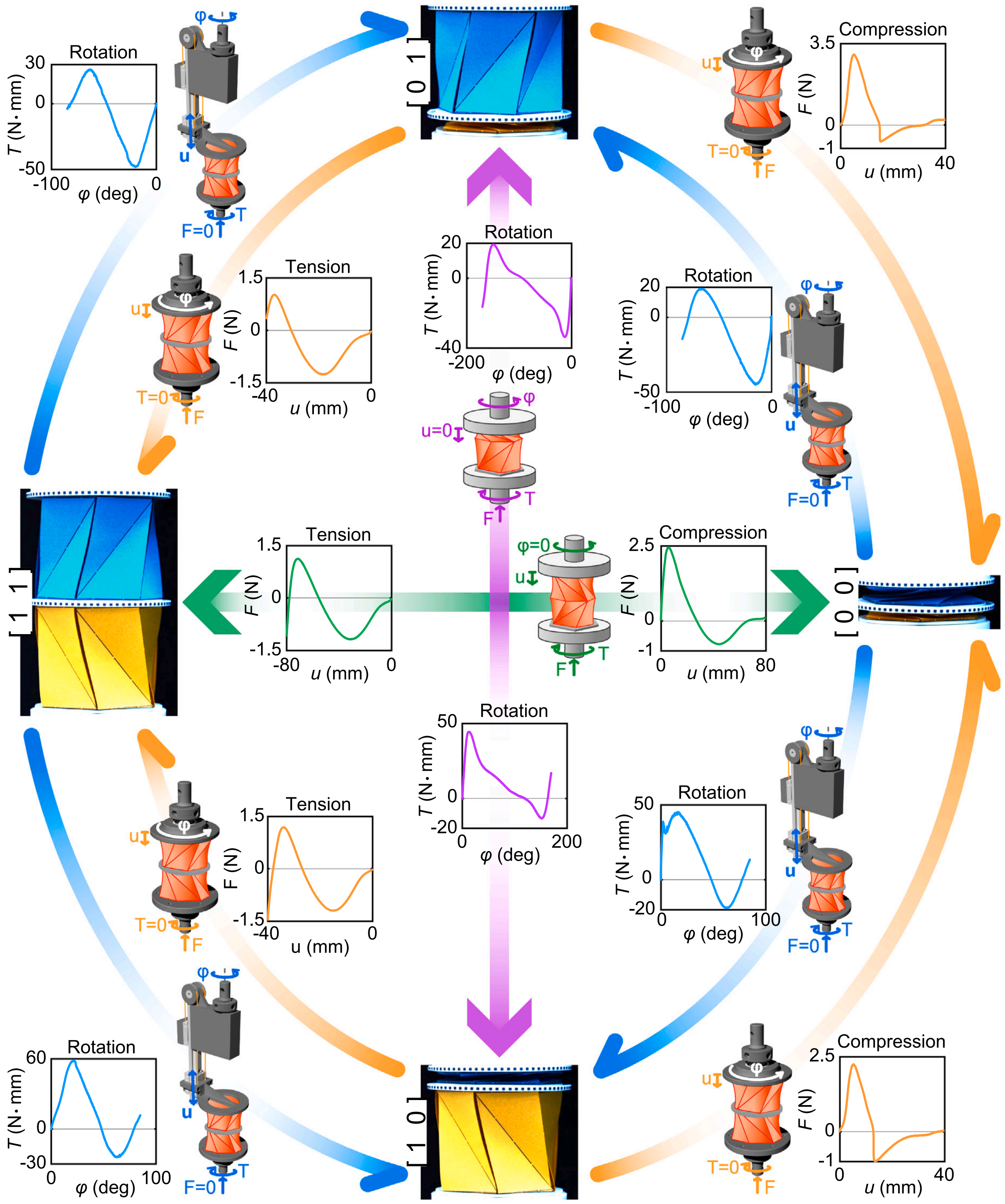

Fig. 2. Mechanical computing based on 2-cell Kresling array using standard and novel testing setups. All the data reported in the plots are collected from the respective experiments.

studies assuming stretchable mountain and valley creases, e.g. Masana and Daqaq (2019), Masana et al. (2020), Lu et al. (2022), Li et al. (2020), and Zhang et al. (2021b).

Nevertheless, both experimental and simulation studies reveal that the folding of panels also influences the mechanical behavior of Kresling structures (Liu and Paulino, 2017; Huang et al., 2022a). This suggests the introduction of the dihedral angles between

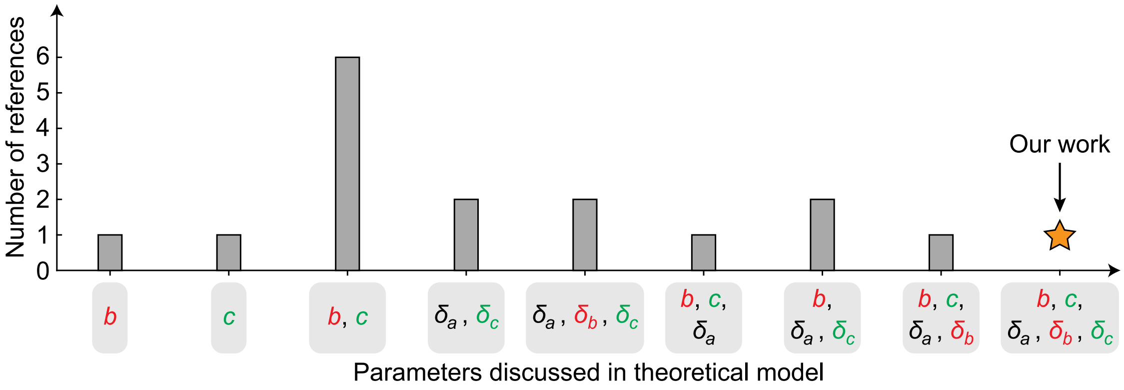

Fig. 3. Summary of previous work on theoretical models, which are based in one or more of the following parameters: b, c, $\delta_a, \delta_b, \delta_c$ with geometric interpretation provided by Fig. 4. For parameter b, see Bhovad et al. (2019); for parameter c, see Cai et al. (2015); for parameters b, c, see Yasuda et al. (2017), Masana and Daqaq (2019), Masana et al. (2020), Lu et al. (2022), Li et al. (2020) and Zhang et al. (2021b); for parameters δ_a, δ_c, see Pagano et al. (2016, 2017); for parameters $\delta_a, \delta_b, \delta_c$, see Huang et al. (2022a,b); for parameters b, c, δ_a, see Yasuda et al. (2019); for parameters b, δ_a, δ_c, see Nayakanti et al. (2018) and Zhang et al. (2021a); for parameters b, c, δ_a, δ_b, see Jin et al. (2022). Our work involves all the five parameters b, c, $\delta_a, \delta_b, \delta_c$.

panels as geometrical parameters to complement the theoretical model. For instance, Pagano et al. (2016) and Pagano et al. (2017) proposed a theoretical model involving two dihedral angles: one between the top polygon and the side triangular panel, and the other between two side triangular panels along a valley crease. However, Huang et al. (2022b) suggested that a Kresling structure without any cutout creases should incorporate all three dihedral angles.

Motivated by our desire to improve upon the aforementioned models and to provide the most simplified model that captures the essence of Kresling mechanics, we present a 5-parameter model that incorporates its representative variable geometric parameters, i.e., two lengths of creases along mountain folds and valley folds, respectively; two dihedral angles between side triangular panels along mountain creases and valley creases, respectively; and one dihedral angle between surface polygons and side triangular panels. The stiffness coefficients of these geometric parameters, embedded in the energy function, can be independently tuned, enabling the theoretical model to accommodate the analysis for various applications.[1]

2.2. *Experimental considerations*

The deformation of a Kresling cell couples axial contraction/expansion and twisting. These unique kinematics challenge standard experimental fixtures capable of a single-degree-of-freedom deformation control. To resolve this issue, Wilson et al. (2013) proposed a compression/tension test on a pair of Kresling cells with opposite chirality, eliminating the twisting degree of freedom on the boundaries.

This experimental work was then extended to Kresling arrays built by multiple pairs of chiral cells (Jules et al., 2022). However, this approach is restricted to an even number of cells and thus cannot capture the folding/deploying behavior of a single Kresling cell. Thus, a new experimental setup, incorporating a rotating base on the loading plate, was introduced to conduct the compression experiment on a Kresling array (Cleveland et al., 2016). This fixture, decoupling two deformation modes, has been used by various researchers investigating Kresling origami, e.g., Nayakanti et al. (2018), Yasuda et al. (2019), Bhovad et al. (2019), Masana and Daqaq (2019), Masana et al. (2020), Zhang et al. (2021a), Huang et al. (2022a) and Yang et al. (2023). However, none of the previous works involved a torque sensor to verify zero torsion under compression loading, which is addressed in the present paper.

There is a dearth of information on how to design a torsion experimental setup that allows free axial deformation. The mechanical testing setups developed in this study address the challenge of decoupling axial contraction/expansion and twisting of Kresling cells in either compression or torsional tests, enabling the simultaneous collection of force and torque data. Verification was achieved through the nearly zero torque and force curves observed in compression and torsional experiments, respectively. These novel setups allow conducting compression and torsion tests on a generic Kresling array with cells of arbitrary chirality.

3. Formulation of the Kresling mechanics problem

The Kresling cell consisting of two identical parallel n-sided equilateral polygons connected by $2n$ repeating triangular panels ($n = 6$ in Fig. 4) can be described by three intrinsic parameters, h_{folded} (the height in the folded configuration), θ_0 (the relative angle between the top and bottom polygons in the initial configuration, i.e., deployed state), and r (the radius of the circumscribed circle of polygon). Here, we choose the parameter $h_{\text{folded}} = 0$. Thus, the height in the initial configuration is calculated by

---

[1] Instead of using detailed finite element model with shell elements, which is very time consuming, one could use the present mode which is simple and effective to gain insights.

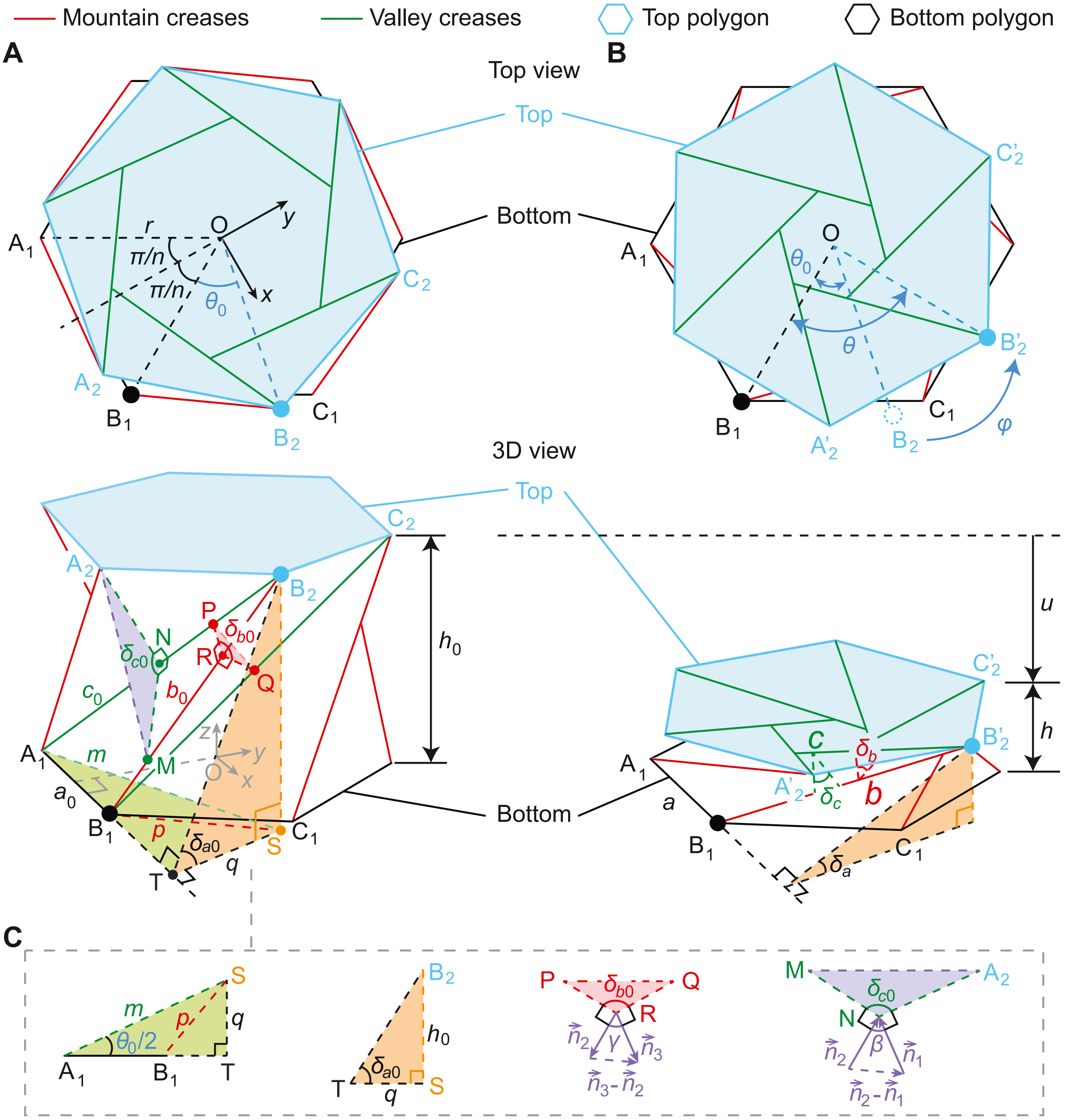

Fig. 4. Geometric configuration of the Kresling origami. The first row shows the top view, the second row shows a perspective view, and the third row shows pertinent details. (A) Schematics of the deployed configuration with geometric parameters and vertices description. (B) Schematics of the folded configuration. (C) The inset triangles illustrate the twisting angle θ_0, and three dihedral angles δ_{a0}, δ_{b0}, δ_{c0}, respectively. The color scheme among figures is consistent (on the first two rows, mountains are red and valleys are green).

$h_0 = r\sqrt{2(\cos\theta_0 - \cos\theta_{\max})}$, where $\theta_{\max} = \pi - (2\pi/n) - \theta_0$ is the relative angle between polygons in the folded configuration (Lang, 2017). The initial lengths, a_0, b_0, and c_0, and dihedral angles, δ_{a0}, δ_{b0}, and δ_{c0}, can be described by n, h_0, θ_0, and r (details are shown in Appendix A.1). Next, we investigate the Kresling geometry in detail, derive its potential energy, and conduct a parametric study to understand its behavior consisting of axial loading with free rotation, and torsional loading with free translation.

3.1. Geometrical interpretation

Assuming that the polygons do not deform, i.e., $a = a_0$ in Fig. 4A and B, we can describe the three lengths, a, $b(u,\varphi)$, and $c(u,\varphi)$, and the three dihedral angles, $\delta_a(u,\varphi)$, $\delta_b(u,\varphi)$, and $\delta_c(u,\varphi)$ in a folding configuration (Fig. 4B) along with two variables, u and φ (see detailed derivations in Appendix A.2). Here, u is the distance between points B_2 and B_2' in z-direction, and φ denotes the twisting angle of the top polygon (i.e., from point B_2 to point B_2') with the bottom polygon fixed. Based on this framework, we derive the following relationships:

$$a = 2r\sin(\pi/n) \tag{1}$$

$$b(u,\varphi) = \sqrt{(h_0-u)^2 + 4r^2\sin^2(\varphi/2+\theta_0/2)} \tag{2}$$

$$c(u,\varphi) = \sqrt{(h_0-u)^2 + 4r^2\sin^2(\varphi/2+\theta_0/2+\pi/n)} \tag{3}$$

$$\delta_a(u,\varphi) = \arctan\frac{(h_0-u)}{2r\sin(\varphi/2+\theta_0/2+\pi/n)\sin(\varphi/2+\theta_0/2)} \tag{4}$$

$$\delta_b(u,\varphi) = \pi - \arccos\frac{(h_0-u)^2\cos(\varphi+\theta_0+2\pi/n) - r^2[\cos(\varphi+\theta_0+\pi/n)-\cos(\pi/n)]^2}{(h_0-u)^2 + r^2[\cos(\varphi+\theta_0+\pi/n)-\cos(\pi/n)]^2} \tag{5}$$

$$\delta_c(u,\varphi) = \pi - \arccos\frac{(h_0-u)^2\cos(\varphi+\theta_0) - r^2[\cos(\varphi+\theta_0+\pi/n)-\cos(\pi/n)]^2}{(h_0-u)^2 + r^2[\cos(\varphi+\theta_0+\pi/n)-\cos(\pi/n)]^2} \tag{6}$$

3.2. Mechanical behavior

Inspired by the bar-and-hinge-model for the Kresling origami cells (Liu and Paulino, 2017), we discretize creases with bar elements and rotational springs. The total elastic energy, U, is a combination of the elastic energy stored in bar elements, U_{bar}, and that provided by rotational springs, U_{rot}. Thus, $U(u,\varphi) = U_{bar}(u,\varphi) + U_{rot}(u,\varphi)$. For the Kresling cell in Fig. 4, we have:

$$U_{bar}(u,\varphi) = \frac{1}{2}n_b k_{s,b}(b(u,\varphi)-b_0)^2 + \frac{1}{2}n_c k_{s,c}(c(u,\varphi)-c_0)^2 \tag{7}$$

$$U_{rot}(u,\varphi) = \frac{1}{2}n_a k_{r,a}(\delta_a(u,\varphi)-\delta_{a0})^2 + \frac{1}{2}n_b k_{r,b}(\delta_b(u,\varphi)-\delta_{b0})^2 + \frac{1}{2}n_c k_{r,c}(\delta_c(u,\varphi)-\delta_{c0})^2 \tag{8}$$

where all the geometric parameters are determined by Eqs. (A.1)–(A.6) and Eqs. (1)–(6). Notice that n_b is the number of mountain creases, n_c is the number of valley creases, n_a is the number of edges of the polygons (top and bottom surfaces), $k_{s,b}$ is the stretching stiffness of mountain creases, $k_{s,c}$ is the stretching stiffness of valley creases, $k_{r,a}$ is the folding stiffness between the side panels and polygons (top and bottom surfaces), $k_{r,b}$ is the folding stiffness between two side panels connected by a mountain crease, and $k_{r,c}$ is the folding stiffness between two side panels connected by a valley crease. Thus, the total elastic energy of a Kresling cell is expressed as:

$$\begin{aligned} U(u,\varphi) &= \frac{1}{2}n_b k_{s,b}(b(u,\varphi)-b_0)^2 + \frac{1}{2}n_c k_{s,c}(c(u,\varphi)-c_0)^2 \\ &+ \frac{1}{2}n_a k_{r,a}(\delta_a(u,\varphi)-\delta_{a0})^2 + \frac{1}{2}n_b k_{r,b}(\delta_b(u,\varphi)-\delta_{b0})^2 + \frac{1}{2}n_c k_{r,c}(\delta_c(u,\varphi)-\delta_{c0})^2 \end{aligned} \tag{9}$$

Previous investigations revealed that the Kresling cell can be controlled by both axial force, F, and torque, T (Yasuda et al., 2017, 2019). Thus, the work done on the cell is calculated by $W(u,\varphi) = \int F(u,\varphi)du + \int T(u,\varphi)d\varphi$. The total potential energy of the Kresling cell, Π, can be expressed using the total elastic energy, U, and work, W, i.e., $\Pi(u,\varphi) = U(u,\varphi) - W(u,\varphi)$. Substituting Eq. (9) into the potential energy expression, we obtain:

$$\begin{aligned} \Pi(u,\varphi) &= \frac{1}{2}n_b k_{s,b}(b(u,\varphi)-b_0)^2 + \frac{1}{2}n_c k_{s,c}(c(u,\varphi)-c_0)^2 + \frac{1}{2}n_a k_{r,a}(\delta_a(u,\varphi)-\delta_{a0})^2 \\ &+ \frac{1}{2}n_b k_{r,b}(\delta_b(u,\varphi)-\delta_{b0})^2 + \frac{1}{2}n_c k_{r,c}(\delta_c(u,\varphi)-\delta_{c0})^2 - \int F(u,\varphi)du - \int T(u,\varphi)d\varphi \end{aligned} \tag{10}$$

Notice that Eq. (10) includes two independent variables, u and φ. Based on the principle of minimum total potential energy, equilibrium is achieved when:

$$\partial\Pi/\partial u = 0,\ \partial\Pi/\partial\varphi = 0 \tag{11}$$

Substituting Eq. (10) into Eq. (11), we calculate the axial force, F, and the torque, T, as follows:

$$\begin{aligned} F(u,\varphi) &= \partial U(u,\varphi)/\partial u \\ &= -(h_0-u)\frac{n_b k_{s,b}(b(u,\varphi)-b_0)}{b(u,\varphi)} - (h_0-u)\frac{n_c k_{s,c}(c(u,\varphi)-c_0)}{c(u,\varphi)} \\ &- \frac{n_a k_{r,a}(\delta_a(u,\varphi)-\delta_{a0})}{2r(\tan^2\delta_a(u,\varphi)+1)\sin(\varphi/2+\theta_0/2+\pi/n)\sin(\varphi/2+\theta_0/2)} \\ &- \frac{2n_b k_{r,b}(\delta_b(u,\varphi)-\delta_{b0})(h_0-u)[\cos(\varphi+\theta_0+2\pi/n)+1]e_1(\varphi)}{\sqrt{1-\cos^2(\pi-\delta_b(u,\varphi))}[(h_0-u)^2+e_1(\varphi)]^2} \\ &- \frac{2n_c k_{r,c}(\delta_c(u,\varphi)-\delta_{c0})(h_0-u)[\cos(\varphi+\theta_0)+1]e_1(\varphi)}{\sqrt{1-\cos^2(\pi-\delta_c(u,\varphi))}[(h_0-u)^2+e_1(\varphi)]^2} \end{aligned} \tag{12}$$

$$\begin{aligned} T(u,\varphi) &= \partial U(u,\varphi)/\partial\varphi \\ &= \frac{n_b k_{s,b}(b(u,\varphi)-b_0)}{b(u,\varphi)} r^2 \sin(\varphi+\theta_0) + \frac{n_c k_{s,c}(c(u,\varphi)-c_0)}{c(u,\varphi)} r^2 \sin(\varphi+\theta_0+2\pi/n) \\ &- \frac{n_a k_{r,a}(\delta_a(u,\varphi)-\delta_{a0})(h_0-u)\sin(\varphi+\theta_0+\pi/n)}{4r(\tan^2\delta_a(u,\varphi)+1)\sin^2(\varphi/2+\theta_0/2+\pi/n)\sin^2(\varphi/2+\theta_0/2)} \\ &- \frac{n_b k_{r,b}(\delta_b(u,\varphi)-\delta_{b0})g_b(u,\varphi)}{\sqrt{1-\cos^2(\pi-\delta_b(u,\varphi))}[(h_0-u)^2+e_1(\varphi)]^2} \\ &- \frac{n_c k_{r,c}(\delta_c(u,\varphi)-\delta_{c0})g_c(u,\varphi)}{\sqrt{1-\cos^2(\pi-\delta_c(u,\varphi))}[(h_0-u)^2+e_1(\varphi)]^2} \end{aligned} \tag{13}$$

where

$$\begin{aligned} g_b(u,\varphi) &= (h_0-u)^2\sin(\varphi+\theta_0+2\pi/n)[(h_0-u)^2+e_1(\varphi)] \\ &\quad + (h_0-u)^2[\cos(\varphi+\theta_0+2\pi/n)+1]e_1'(\varphi) \\ g_c(u,\varphi) &= (h_0-u)^2\sin(\varphi+\theta_0)[(h_0-u)^2+e_1(\varphi)] + (h_0-u)^2[\cos(\varphi+\theta_0)+1]e_1'(\varphi) \\ e_1(\varphi) &= r^2[\cos(\varphi+\theta_0+\pi/n)-\cos\pi/n]^2 \\ e_1'(\varphi) &= -r^2\sin(2\varphi+2\theta_0+2\pi/n)+2r^2\cos(\pi/n)\sin(\varphi+\theta_0+\pi/n) \end{aligned}$$

The prime in $e_1'(\varphi)$ denotes derivative.

3.3. Targeted parametric study

The stretching stiffness of the creases and the folding stiffness between panels contribute greatly to the total elastic energy function in Eq. (9). The stiffness terms in Eq. (9) can be defined using the following expressions.

$$k_{s,b} = k_s/b_0,\ k_{s,c} = k_s/c_0 \tag{14}$$

$$k_{r,a} = k_r a_0,\ k_{r,b} = k_r b_0,\ k_{r,c} = k_r c_0 \tag{15}$$

where k_s, measured by $(\mathrm{N\ mm^{-1}})\mathrm{mm}$, denotes the normalized stretching stiffness of the creases, and k_r, measured by $\mathrm{N\ mm(rad\ mm)^{-1}}$, denotes the rotational stiffness of the crease per unit length. For a constant k_s, e.g., $k_s = 50\ (\mathrm{N\ mm^{-1}})\mathrm{mm}$, we vary k_r from 0 to $1.25\times10^{-2}\ \mathrm{N\ mm(rad\ mm)^{-1}}$, and study how the stiffness (k_r) influences the monostable and bistable behaviors under two types of loading conditions, i.e, axial loading with free-rotation, and torsional loading with free-translation. We choose $n = 6$, $r = 30$ mm, and $\theta_0 = 30°$ as the initial geometry parameters – see Fig. 5.

3.3.1. Axial loading with free-rotation

Here, the cell deforms in the axial direction and rotates freely. Thus, the torque defined in Eq. (13) is zero. We have:

$$\partial U(u,\varphi)/\partial\varphi = 0 \tag{16}$$

For a given stiffness k_r, we can obtain the relationship, $\varphi = f_F(u)$, by solving Eq. (16) – see details in Appendix A.3. Based on this relationship, we can calculate crease lengths, $b(u,\varphi)$ and $c(u,\varphi)$, and dihedral angles, $\delta_a(u,\varphi)$, $\delta_b(u,\varphi)$, and $\delta_c(u,\varphi)$, using Eqs. (2)–(6). Then we can calculate the total elastic energy, $U(u,\varphi)$, and axial force, $F(u,\varphi)$, using Eqs. (9) and (12), respectively.

Based on this theoretical investigation, the Kresling cell has two zero-energy kinematic stable configurations when k_r is zero (Fig. 5 A(left)). In this case, panel stretching, represented by the deformation of mountain and valley creases (Fig. 5A(middle)), dominates the stored energy. As k_r increases, the position of the second stable state changes. This is due to the monotonically increasing energy contributed by panel folding. Fig. 5A(right) indicates that the dihedral angles between panels change monotonically. The stable states position can be obtained using the following stationary condition:

$$\partial U/\partial u = 0,\ \partial^2 U/\partial u^2 > 0 \tag{17}$$

The detailed solution scheme solving Eq. (17) is listed in Appendix A.3, and results are summarized in Table 1. Note that Eq. (17) has a single root when $k_r > 1.25\times10^{-2}\ \mathrm{N\ mm(rad\ mm)^{-1}}$. This indicates that the Kresling cell becomes monostable.

3.3.2. Torsional loading with free-translation

In this case, the rotational degree of freedom (DOF) is under control, but the vertical displacement DOF is free. Thus, the axial force in Eq. (12) is zero and we have:

$$\partial U(u,\varphi)/\partial u = 0 \tag{18}$$

By solving Eq. (18), we derive the relationship, $u = f_T(\varphi)$ (see details in Appendix A.3). Then we can compute crease lengths, $b(u,\varphi)$ and $c(u,\varphi)$, and dihedral angles, $\delta_a(u,\varphi)$, $\delta_b(u,\varphi)$, and $\delta_c(u,\varphi)$, by using Eqs. (2)–(6), and the total elastic energy, $U(u,\varphi)$, and the torque, $T(u,\varphi)$, using Eqs. (9) and (13).

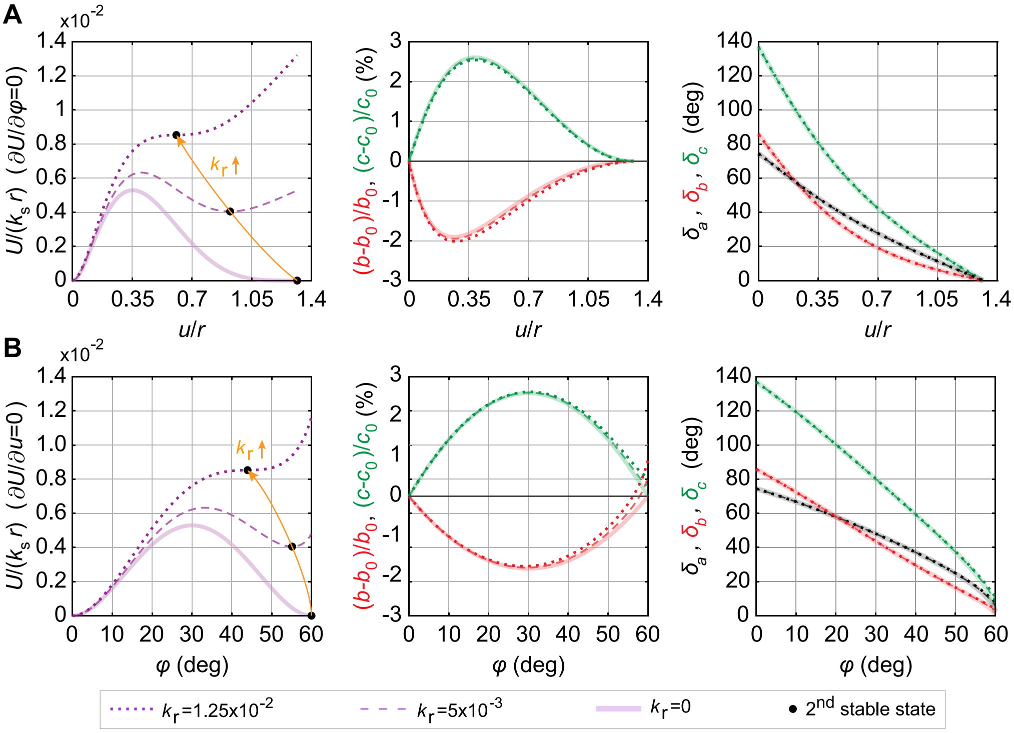

Fig. 5. Mechanics of the Kresling cell considering two loading conditions, i.e., axial compression (free-rotation) and torsion (free-translation). (A) Axial compression loading condition. The stored strain energy of the Kresling cell versus the vertical displacement of any vertices on the top hexagonal plane (left); change of lengths for the mountain creases versus vertical displacement (middle); three dihedral angles versus the vertical displacement (right). The strain energy ($U/k_s r$) and displacement (u/r) are normalized in the parametric analysis. Black dots indicate positions of the 2nd stable states. Multiple dashed and shaded lines represent the solution considering a range of stiffness k_r from 0 to 1.25×10^{-2} N mm(rad mm)$^{-1}$. The line colors, i.e., black, red, and green, are consistent with the color code used for edges and creases in Fig. 4. (B) Torsional loading condition. The strain energy versus the twisting angle of the top hexagonal plane (left); change of lengths for the mountain and valley creases versus the twisting angle (middle); three dihedral angles versus the vertical displacement (right).

Table 1
Position of the 2nd stable state considering a range of stiffness k_r.

k_r (N mm(rad mm)$^{-1}$)	$U/(k_s r)$	u/r	φ (deg)
1.25×10^{-2}	8.5×10^{-3}	0.6	44
5×10^{-3}	4.1×10^{-3}	0.9	55
0	0	1.3	60

As shown in Fig. 5B(left), the trend of the elastic energy landscape is similar to that observed in the axial compression loading condition. However, the changes of geometric parameters in the torsion loading condition exhibit distinct behavior compared to those in the compression loading condition. As illustrated in Fig. 5B(middle), the mountain and valley creases do not return to their initial lengths unless k_r is zero. For a case with non-zero k_r, an imposed twist angle leads to a non-zero height in the folded state. This implies that the Kresling cell under torsion loading condition can only achieve a completely folded configuration with zero height when k_r is zero. Furthermore, we can calculate the position of stable states under a torsion loading condition using the following conditions:

$$\partial U/\partial \varphi = 0,\ \partial^2 U/\partial \varphi^2 > 0 \tag{19}$$

The solution of Eq. (19) satisfies the conditions in Eq. (17) as expected. This observation justifies that the positions of stable states for standard Kresling origami are independent of loading conditions.

3.4. Comparative analysis

We observe that the number of parameters influences the shape of the Kresling origami energy landscape. Thus, we compare the 5-parameter energy analysis with the 4-, 3-, or 2-parameter analyses in Fig. 6. If only two parameters (i.e., lengths of mountain and valley creases) are used, the stored energy at the 2nd stable state will always be zero. When we add dihedral angles (along creases) as additional parameters into the formulation, the location of the 2nd stable state is allowed to vary, including a non-zero base energy. Furthermore, the 5-parameter model provides a more convenient means to program the magnitude of the base energy.

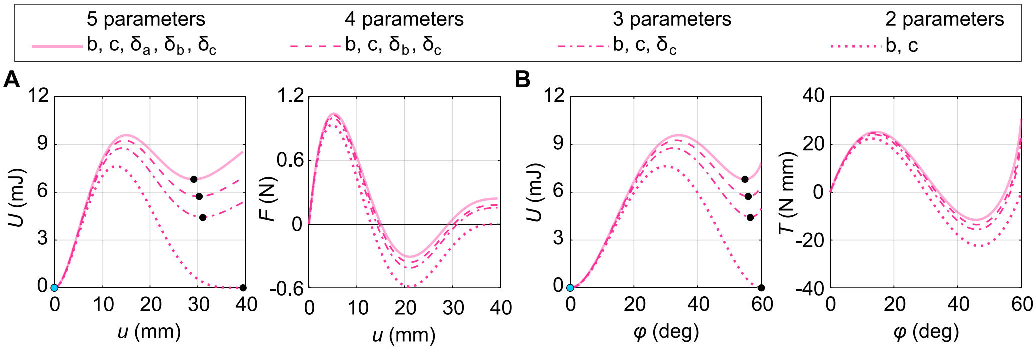

Fig. 6. Results calculated by 5-parameter (b, c, δ_a, δ_b, δ_c), 4-parameter (b, c, δ_b, δ_c), 3-parameter (b, c, δ_c), and 2-parameter (b, c) analyses. (A) Compression loading condition. (B) Torsional loading condition. The geometric parameters are based on the $\varphi_{\max} = 60°$ cell. The stiffness parameters are from the experiments in Appendix D. The blue dot represents the 1st stable state, and the black dots denote the 2nd stable state.

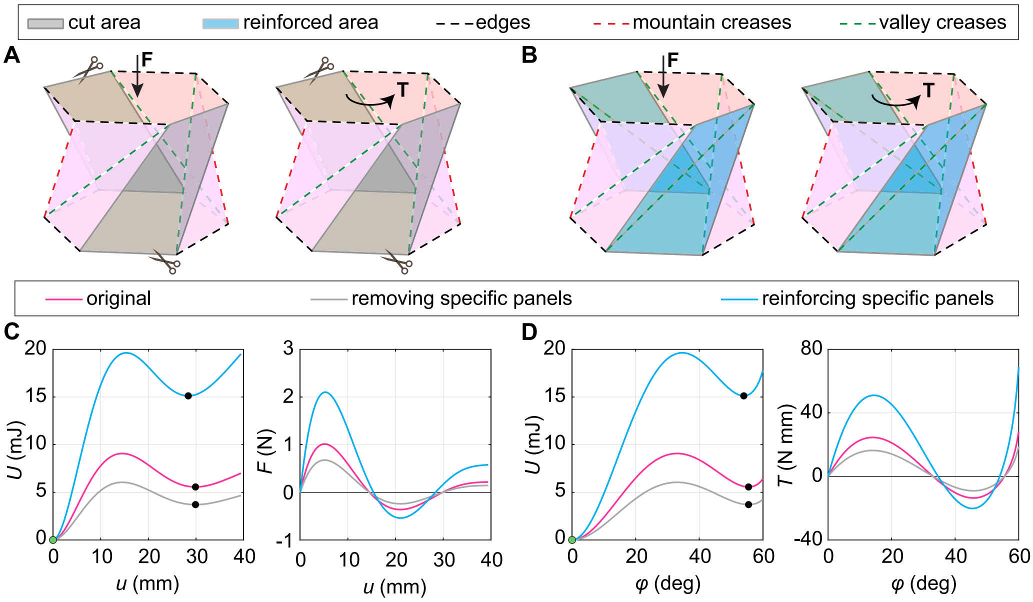

Fig. 7. Comparison between the original Kresling cell and the cell with reinforcing or removing specific panels. Schematic of specimens with (A) cutting side panels or (B) reinforcing side panels. Theoretical results of (C) axial loading with free-rotation and (D) torsional loading with free-translation. The green dot represents the 1st stable state, and the black dots denote the 2nd stable state.

3.5. Effects of removing/reinforcing side panels

Based on the 5-parameter formulation, we further analyze the effect of removing/reinforcing specific panels. Such operations lead to shape changes on the energy landscape. Moreover, adding reinforced panels varies the location of the 2nd stable state, while removing panels has no influence on the location of the 2nd stable state.

Fig. 7A and B illustrate the effect of cutting/reinforcing panels on two opposite sides (to preserve symmetry). In the case of removing panels, the number of creases reduces in the formulation, leading to shape changes on the energy landscape. Since the stretching stiffness k_s and the rotational stiffness k_r are not changing, the location of the 2nd stable state remains the same. In the case of reinforcing panels, the thickness (t) is doubled at the reinforced area. Since $k_s = EA = E\pi(t/2)^2$, then it scales with t^2. The rotational stiffness k_r scales with the flexural rigidity of the panel, $Et^3/12(1-\upsilon^2)$, i.e., the stiffness k_r scales with t^3. Thus, k_r and k_s vary differently at the reinforced area depending on the thickness t, which leads to changes on both the energy landscape and the location of the 2nd stable state (Fig. 7C and D).

4. Fabrication and experiments

To fabricate the experimental Kresling specimens, we used 0.4 mm-thick composite material for all panels. The composite material consists of two layers of paper on the top and bottom, with a central layer of 3M adhesive transfer tape. To create the

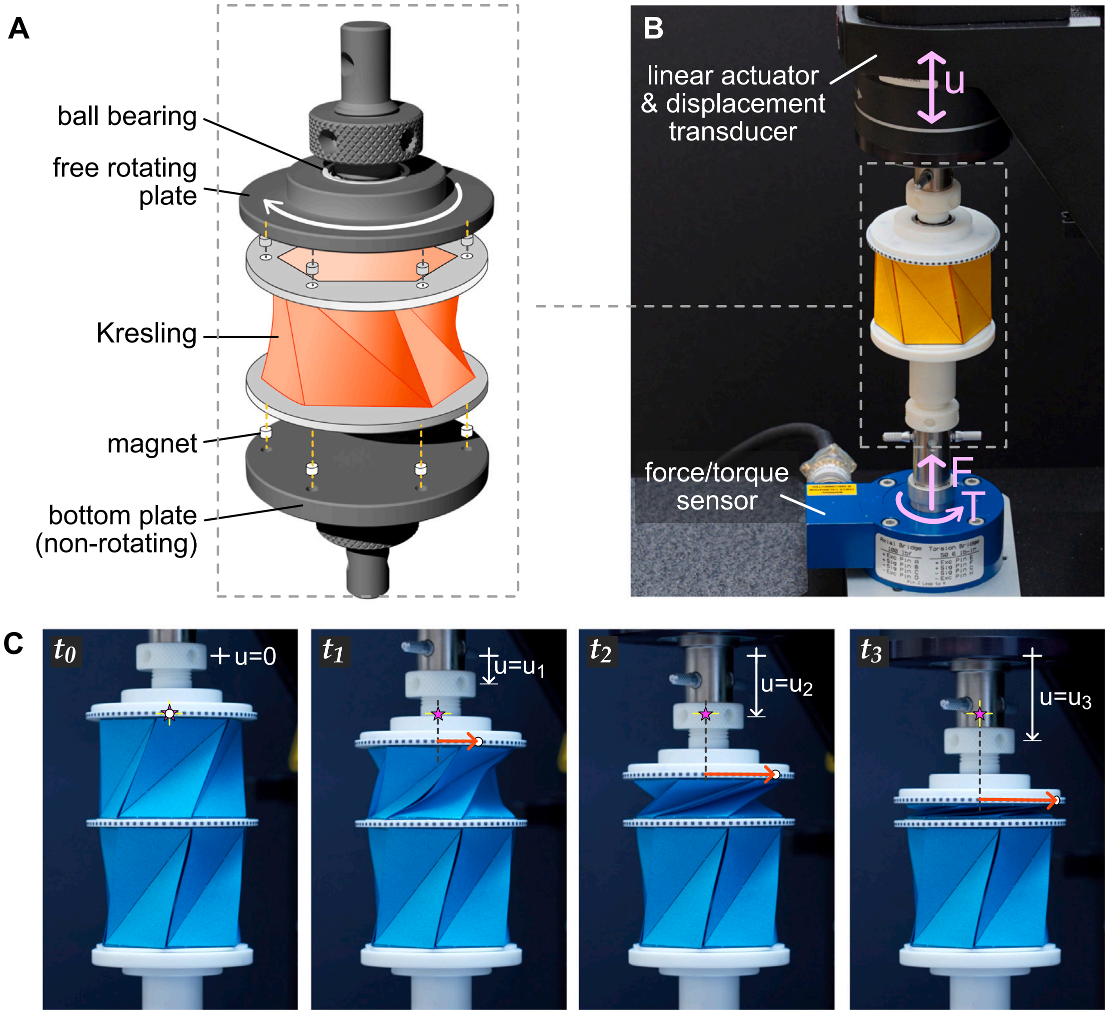

Fig. 8. Details of the setup designed for conducting compression experiments on Kresling origami, equipped with a free-rotating fixture. (A) Schematics and (B) a photograph of the actual setup mounted on an Instron loading frame machine. (C) Snapshots extracted from the record of the experiment at different times illustrating the working principles of the setup. Compression on the Kresling array is achieved by imposing the axial displacement u, indicated by white arrows, using a loading frame machine. The fixture enables free rotation, facilitating the natural twisting of the Kresling, as indicated by the red arrows.

Table 2
Parameters of experimental specimens.

$\varphi_{\max}$ (deg)	n	r (mm)	θ_0 (deg)	h_0 (mm)
60	6	30	30	39.48
90	6	30	15	46.95

creases, we removed the top and bottom layers of paper from the composite material using the laser cutter and were left with the central layer of 0.17 mm-thick tape. In addition, we made cuts along the mountain creases to enhance the folding process. More detailed information can be found in Appendix B.

As shown in Figs. 8 and 9, special fixtures were 3D printed and prepared for installation in the Instron machine. These fixtures have an arrangement of magnets that connect to 3D-printed thin polygonal plates with matching magnets. These polygonal plates are glued to the top and bottom of the Kresling array (for simplicity, the aforementioned figures display only one Kresling unit) that will be tested. The patterned material sheet was initially assembled to the folded configuration ($h = h_{\text{folded}} = 0$) of the Kresling cell. The folded Kresling cell is then deployed using the Instron machine. In this investigation, our experimental studies involved two types of Kresling cells defined by the parameter $\varphi_{\max}$. The specific parameters of the experimental specimens are outlined in Table 2. Further details are provided below.

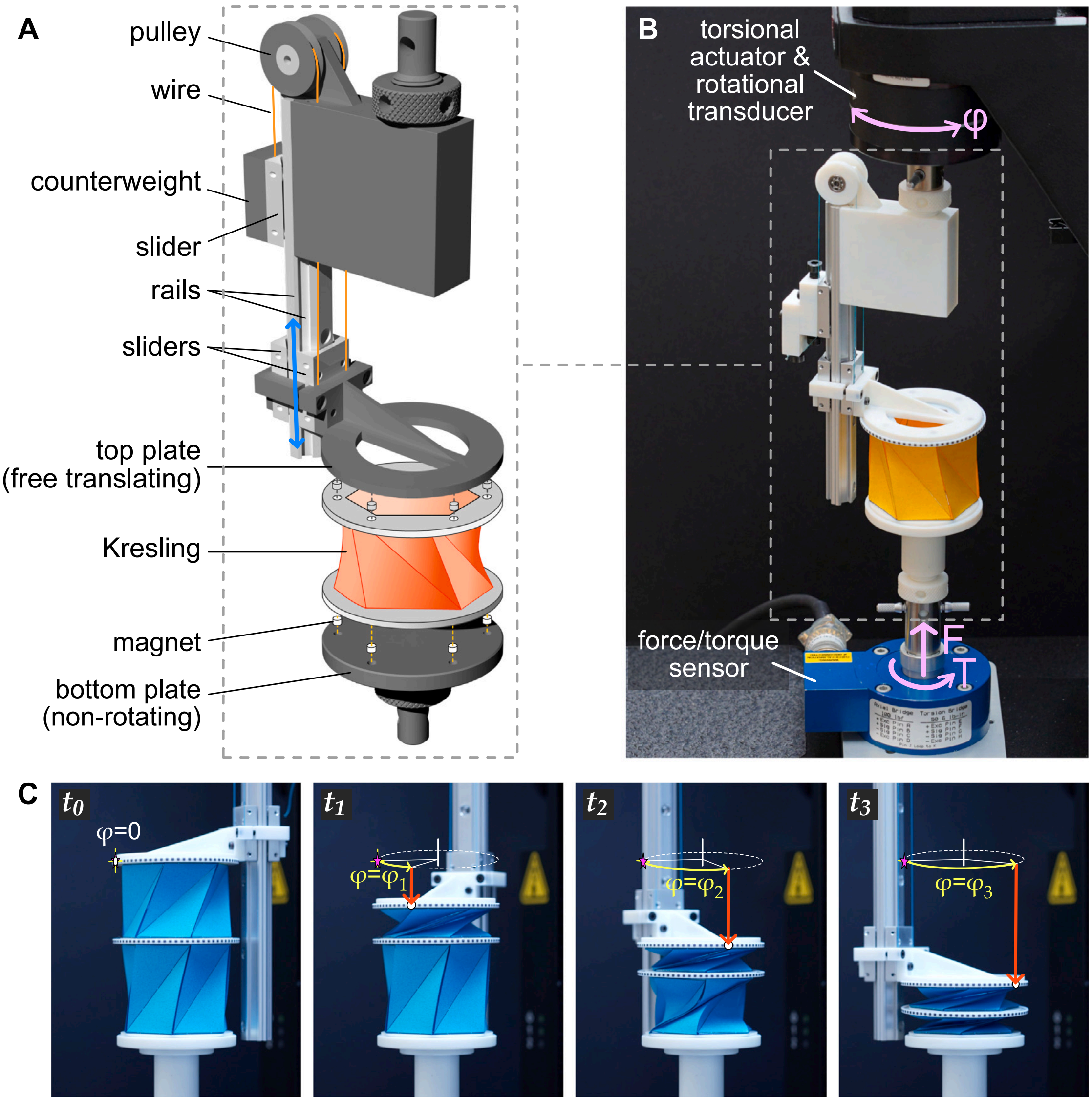

Fig. 9. Details of the setup designed for conducting torsional experiments on Kresling origami, equipped with a free-translating fixture. (A) Schematics and (B) a photograph of the actual setup mounted on an Instron loading frame machine. (C) Snapshots extracted from the record of the experiment at different times illustrating the working principles of the setup. Twisting in the Kresling array is accomplished by applying a rotation φ, as indicated by yellow arrows, using a loading frame machine. The fixture is connected to a linear slide system that enables unrestricted translation, allowing the Kresling array to undergo axial folding without constraints, as indicated by the red arrows.

4.1. Experimental setups

The intrinsic kinematics of the Kresling cell couples axial contraction/expansion and twisting. To investigate this phenomenon, we have designed two distinct experimental configurations that decouple those deformation modes. Thus, the experimental setups allow either compression or torsional tests to be conducted on individual Kresling cells as well as generic Kresling arrays. The arrays can be composed of either an odd number of cells, or an even number of cells, without any constraint on the chiral arrangement of any cell or group of cells. Both setups comprise two fixtures that connect the top and bottom surfaces of the Kresling origami to the Instron loading frame machine (Model 68SC-5 Single Column Testing System), via small shafts, as illustrated by Fig. 8. Both fixtures are equipped with multiple miniaturized magnets, ensuring precise and secure connections between the Kresling and the loading frame, as in Figs. 8 and 9. In both setups, the bottom fixture is the same and effectively restrains both rotational and axial movements, preventing any undesired rigid motion of the Kresling samples during the tests. Figs. 8C and 9C show the snapshots extracted from the movies recorded during the experiments. With the addition of these snapshots, we aim to enhance the clarity of the working principles of the setups. During the tests, we record the axial force and twisting moment using a force/torque sensor (Biaxial Load

Cell ±445 N, ±5.65 N m). Additionally, the axial displacement is monitored through a displacement transducer mounted within the loading frame, which measures the vertical movement of the top cantilevered cross-head of the loading frame.

4.1.1. *Free-rotating fixture for compression experiments*

Within this setup configuration, the top fixture allows for free rotation, enabling the natural twisting of the Kresling structure throughout the folding and unfolding process induced by compression or tension loading. The free rotation capability of the top fixture is achieved through the incorporation of a ball bearing (SKF 608 SKF 8 × 22 × 7) into the top plate, as shown in Fig. 8.

4.1.2. *Free-translating fixture for torsional experiments*

We created a dedicated fixture to enable twist of the Kresling structure while allowing it to undergo axial folding and unfolding without constraint. This capability was achieved through the utilization of a linear rail system equipped with sliders, as illustrated in Fig. 9. The freely translating plate is connected to two rails through the use of two sliders. This approach was adopted to minimize rigid motion between the sliders and the rails, thus reducing frictional effects during testing. To counterbalance the weight of the freely translating top plate, we integrated a pulley system into the fixture. This measure is crucial for precisely capturing the bistable nature of the Kresling, as the weight of the top plate would otherwise exert force on the top surface of the Kresling, thus potentially affecting the accuracy of the experiment.

5. Results and discussion

With the introduction of these new experimental setups shown in Figs. 8 and 9, we are able to program loading conditions on a multi-cell Kresling array, leading to various folding sequences. First, we investigate the new experimental setups using a single cell. Next, we explore multiple loading conditions for Kresling arrays comprised of two cells, each with different geometric parameters and either identical or opposite chirality. We choose 0.25 mm/s for the compression experiment and 0.5 deg/s for the torsional experiment. The details of the loading rate analysis are shown in Appendix C.

5.1. *Experiments on single Kresling cell*

We conduct axial compression and torsional experiments on Kresling cells with $\varphi_{\max} = 60°$ and $\varphi_{\max} = 90°$ to both validate the theoretical model and investigate their mechanical behavior. The compression and twisting tests are shown in Fig. 10A and B, respectively. We measure both force and torque data using the force/torque sensor of the test machine. The torque and force curves in Fig. 10A and B, respectively, verify the effectiveness of our free-rotating and free-translating fixtures, respectively, ignoring the little difference between experiment curves and zero due to fabrication and other errors. Notably, negative force and torque are obtained from the free-rotating compression and free-translating torsional experiments (Fig. 10), which result from the bistability of the Kresling cell.

We then proceed to compare the experimental results with the theoretical model discussed in Section 3. To predict the mechanical properties of the Kresling cells, we conducted a material experiment (see Appendix D) on the composite material to determine the elastic modulus, which was found to be $E = 1503.27$ MPa. Since we assume that k_s in Eq. (14) is equal to EA and A is the cross-section area of the bar element, it is necessary to propose a calculation method of A related to the fabrication process of different creases. Here, the valley creases are modeled by cylindrical bar elements with a radius $t/2$ ($t = 0.4$ mm represents the thickness of the composite material), leading to A rewritten as $A_c = \pi(t/2)^2$. However, the mountain creases were cut in the fabrication process. Thus, we use cylindrical bar elements with smaller diameters than valley creases to model mountain creases and rewrite A as $A_b = \pi(t/7)^2$, where $t/7$ is the radius of bar element of mountain creases. Substituting A_b and A_c into $k_s = EA$, we can re-write Eq. (14) as follows.

$$k_{s,b} = (EA_b)/b_0,\ k_{s,c} = (EA_c)/c_0 \tag{20}$$

Moreover, we present a crease stiffness experiment to determine the normalized rotational stiffness of creases (details are depicted in Appendix D), resulting in $k_r = 0.0054$ N mm(rad mm)$^{-1}$. Based on the above material parameters, the theoretical calculations can be performed by substituting Eqs. (15) and (20) into Eqs. (9), (12), and (13) (see Fig. 10A and B).

A reasonably good match is found when comparing the theoretical results with the experimental data, despite some differences between the curves. These differences are attributed to varying deformations between the panels in the actual test specimens and the simplification due to the use of bar elements in the theoretical model. Furthermore, the elastic energy curves in Fig. 10A and B reveal a significant energy barrier for both Kresling cells with $\varphi_{\max} = 60°$ and $\varphi_{\max} = 90°$ under the two different loading conditions. This feature presents an opportunity to design a multi-cell Kresling array with controllable folding paths.

5.2. *Experiments on two-cell Kresling array*

We present two types of two-cell Kresling arrays designed to study controllable folding paths. Detailed geometric parameters for these arrays are provided in Table 2. Here, we define that the right-handed chiral Kresling cell can be folded using counterclockwise torsion, while the left-handed one can be folded by clockwise torsion. Thus, the first array consists of a $\varphi_{\max} = 60°$ Kresling cell with right-handed chirality and a $\varphi_{\max} = 90°$ Kresling cell with the same chirality. The second array consists of a $\varphi_{\max} = 60°$ Kresling cell

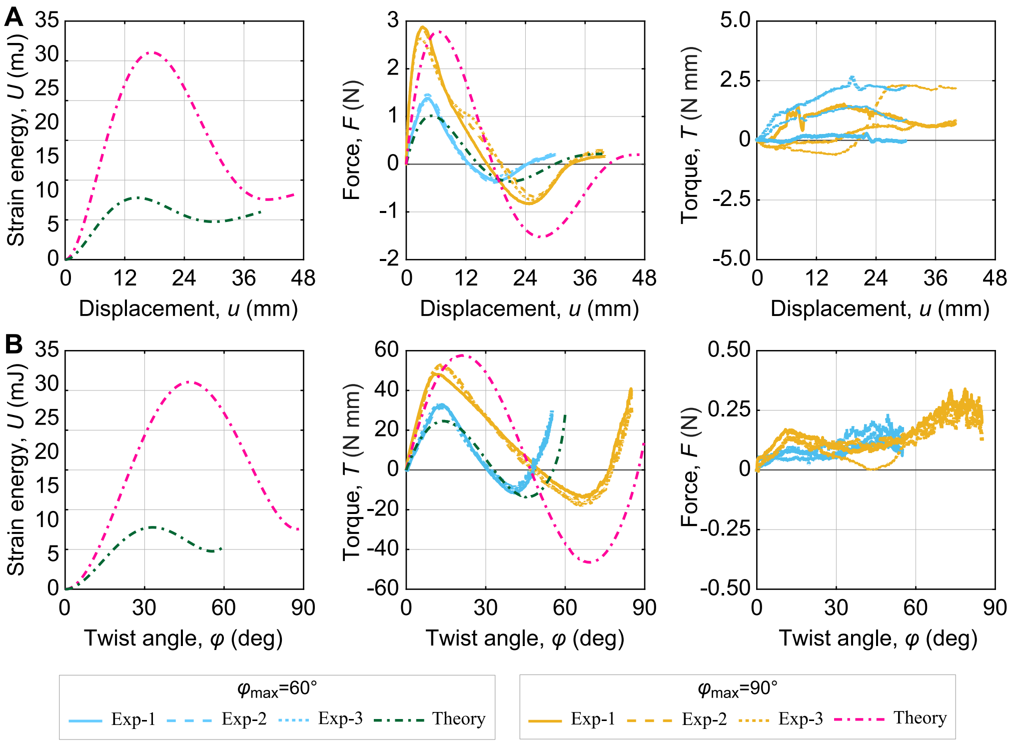

Fig. 10. Theoretical and experimental results of the single Kresling cell testing considering two loading conditions, i.e., compression (free-rotation) and twist (free-translation). Here, two Kresling designs are investigated, i.e, $\varphi_{\max} = 60°$ and 90°. (A) Compression loading condition. The theoretical strain energy of the Kresling cell versus the vertical displacement of any vertices on the top hexagonal plane (left); force applied on the top plane versus vertical displacement (center); torque measured under compression loading (right). (B) Torsional loading condition. The strain energy versus the twisting angle of the top hexagonal plane (left); torque applied on the top plane versus the twisting angle (center); force measured under rotational loading (right). The theoretical torque (right plot in (A)) and force (right plot in (B)) are zero.

with right-handed chirality and a $\varphi_{\max} = 90°$ Kresling cell with opposite chirality. The different arrangement of chiral Kresling cells leads to various folding paths under torsional loading conditions.

5.2.1. *Kresling array consisting of two cells with same chirality*

We consider a Kresling array composed of two identical chiral cells and conduct two experiments. First, we perform an axial compression experiment with 75 mm displacement range (Fig. 11A), and then a counterclockwise torsional experiment with 140° twisting angle (Fig. 11B). Notice that both the torque curve in Fig. 11A and the force curve in Fig. 11B are close to zero, which indicates the effective functioning of the free-rotating fixture and free-translating fixture in the experiments for the array composed of two identical chiral cells.

The force and torque curves reveal that the mechanical properties of Kresling cell within the array qualitatively match those of the single cell. The force curve in Fig. 11A exhibits three distinct zero points (red-colored) corresponding to three stable states, denoted as configurations I, III, and V, under a compression loading condition. Compared with the single-cell experiments, the three stable states of the Kresling array are a combination of the two stable states of the top cell and those of the bottom cell. The same behavior is observed in the torsion loading experiment depicted in Fig. 11B. These consistent findings in different loading conditions indicate that the Kresling array, consisting of two identical chiral cells, follows the same folding process regardless of the applied load.

5.2.2. *Kresling array consisting of two cells with opposite chirality*

In the investigation of a Kresling array composed of opposite chiral cells, we first conduct a free-rotating compression experiment using the same displacement as the experiment on the Kresling array consisting of identical chiral cells (Fig. 12A). The force and torque curves demonstrate that the Kresling array with opposite chiral cells exhibits similar mechanical behaviors and folding paths as the array with identical chiral cells in the compression experiment.

Secondly, we introduced a two-step torsional experiment starting with a counterclockwise torsional loading condition to the Kresling array with two opposite chiral cells (Fig. 12B). In this experiment, we defined that step 1 is a counterclockwise torsional experiment with 58° twisting angle, and step 2 is a clockwise torsional experiment with 85° twisting angle. Here, we define that

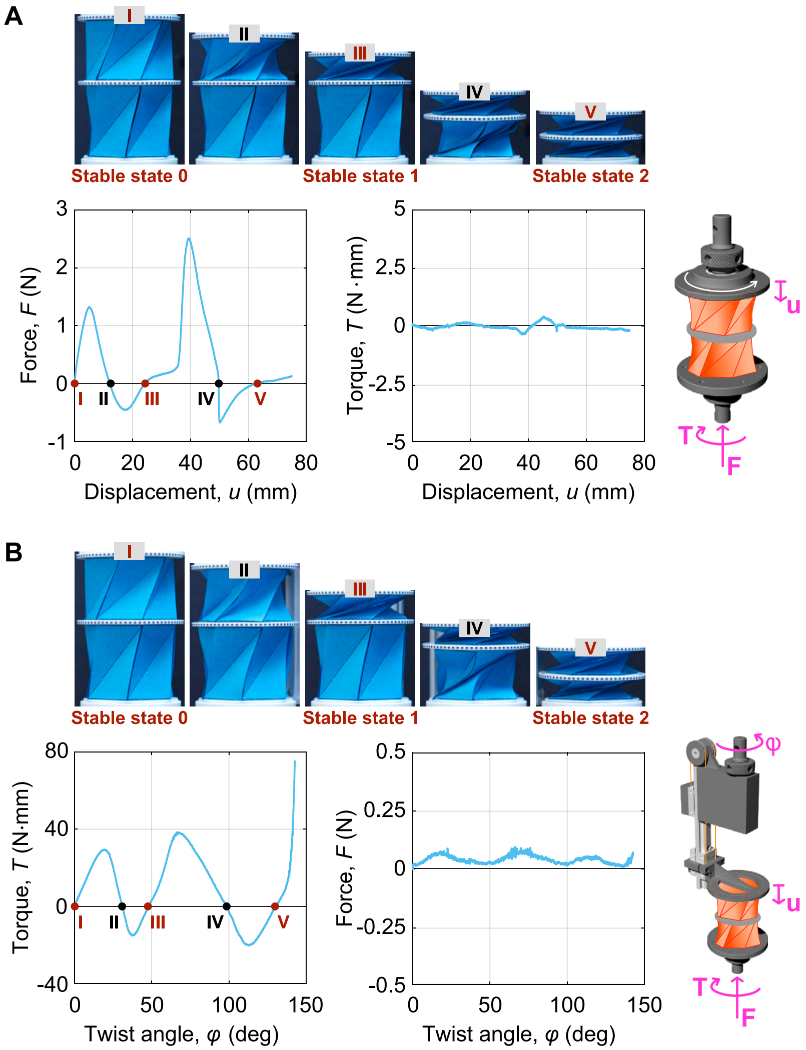

Fig. 11. Experimental results of the Kresling array consisting of two identical chiral cells. (A) Axial compression (free-rotation) experimental results. The representative deformed configurations (top). Force applied to the top of the array versus vertical displacement of the top hexagonal plane (bottom-left). Torque measured under compression loading condition (bottom-center). Schematic of the boundary conditions for compression loading condition (right). (B) Torsional (free-translation) experimental results. The representative deformed configurations (top). Torque applied on the top of the array versus twisting angle of the top hexagon plane (bottom-left). Force measured under torsional loading condition (bottom-center). Schematic of the boundary conditions for torsional loading condition along a counterclockwise direction (right).

clockwise torsion is negative while counterclockwise torsion is positive in the torque curves of a two-step torsional experiment. From configurations and torque curve in Fig. 12B, we observe that only the $\varphi_{\max} = 60°$ Kresling cell folded and deployed under this loading condition. This outcome results from the fact that deploying a $\varphi_{\max} = 60°$ Kresling cell with right-handed chirality is easier than folding a $\varphi_{\max} = 90°$ one with left-handed chirality using clockwise torsional loading condition, i.e., a lower energy is required for folding a $\varphi_{\max} = 60°$ cell than deploying a $\varphi_{\max} = 90°$ one.

Finally, we present a two-step torsional experiment starting with a clockwise torsional loading condition on the Kresling array composed of two opposite chiral cells (Fig. 12C). The 1st step is a clockwise torsional experiment with 88° twisting angle, while the 2nd step is a counterclockwise torsional experiment with 55° twisting angle. The drops in the torque curve are caused by the panel buckling of the $\varphi_{\max} = 60°$ cell. Ignoring these buckling responses, we conclude from Fig. 12C that the Kresling cells in this torsional experiment have similar mechanical behaviors with the single-cell experimental results. According to the configurations captured in the experiment, the $\varphi_{\max} = 90°$ Kresling cell with left-handed chirality is folded before the $\varphi_{\max} = 60°$ one with right-handed chirality is folded, which overcomes the influence of lower energy barrier in Fig. 12B.

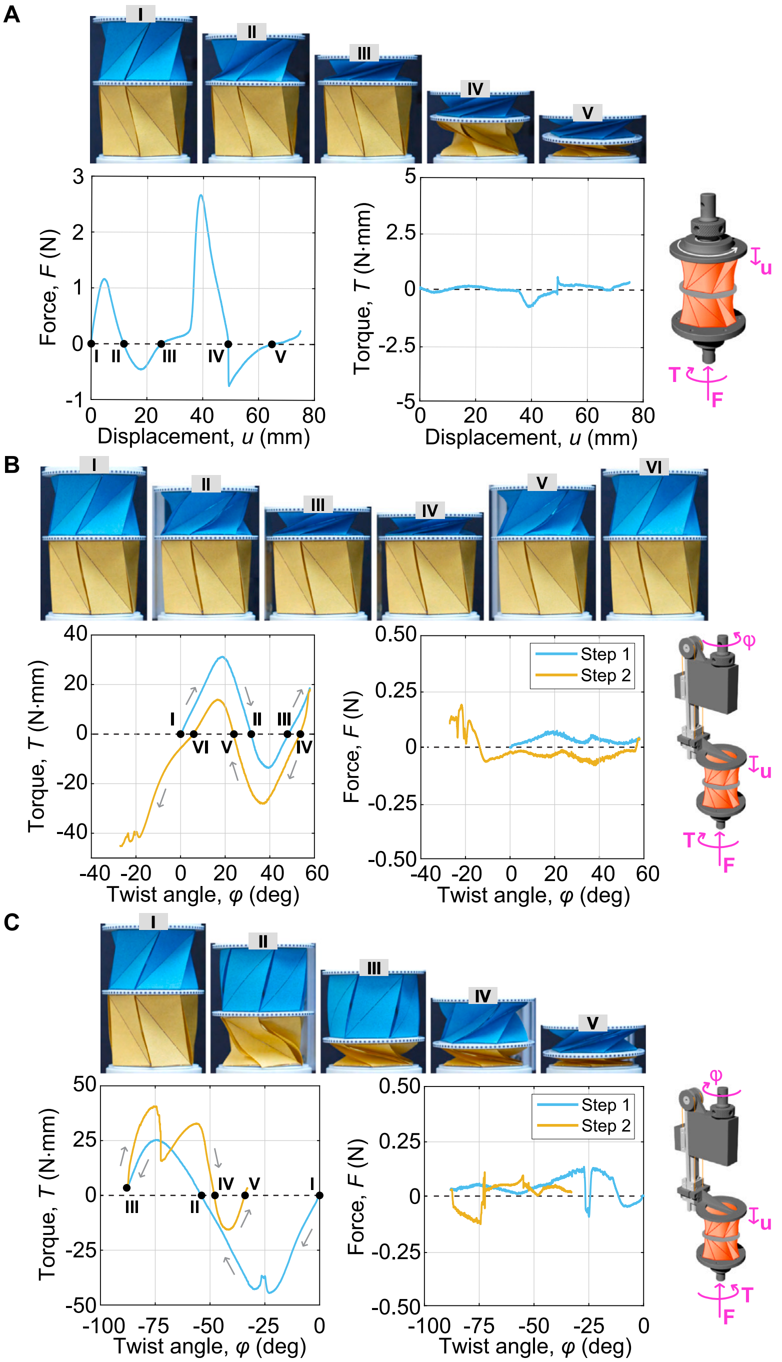

Fig. 12. Experimental results of 2-cell Kresling array with opposite chirality under compression (free-rotation) and torsional (free-translation) loading conditions. The folding configurations, force, and torque curves under (A) the compression loading condition and (B) (C) the torsional loading conditions. The loading conditions are illustrated in the schematics on the right. The specimen in (B) is folded by a counterclockwise torsion in step 1 and a clockwise torsion in step 2. Conversely, the specimen in (C) is folded by a clockwise torsion in step 1 and a counterclockwise torsion in step 2. Grey arrows show the direction of loading.

Comparing the results in Figs. 11 and 12, we notice that a Kresling array with identical chiral cells has only one folding path under different loading conditions. In contrast, a Kresling array with opposite chiral cells possesses multiple folding paths, which can be controlled by different loading conditions, e.g., clockwise torsion and counter-clockwise torsion.

5.2.3. Instability/Buckling effects in two-cell Kresling array analysis

In the torsional experiment of the 2-cell array with opposite chirality (Fig. 12C), we observed panel buckling in the $\varphi_{\max} = 60°$ cell (blue color) changing from configuration I to configuration II. Then, the buckled panel recovered during deformation from configuration III to configuration IV. More details about buckling effects are presented in Appendix E.

6. Concluding remarks

The Kresling pattern possesses a rich mechanics behavior, which is associated to its non-rigid origami behavior coupling axial deformation and twist. On the theoretical mechanics front, we presented a comprehensive model incorporating the five representative geometrical parameters of the Kresling origami cell into the corresponding energy function, which is applicable to either single cell or multi-cell arrays. On the experimental mechanics front, we have created two experimental configurations that decouple the deformation modes (axial deformation and twist) of the Kresling pattern. The first experimental configuration consists of a free-rotating fixture for tension/compression experiments, and the second experimental setup consists of a free-translating fixture for torsional experiments. The aforementioned experimental setups can be used to test Kresling arrays composed of either an odd number of cells, or an even number of cells, without any constraint on the chiral arrangement of any cell or group of cells.

When testing the 2-cell Kresling array, we found that if the cells have different energy barriers but the same chirality, then there is only one folding path under different loading conditions. In contrast, if the Kresling cells have opposite chirality, then there are multiple folding paths, which can be controlled by different loading conditions, e.g., clockwise torsion and counter-clockwise torsion. Thus, the interplay between energy barriers and chirality provides the means to control mechanical behavior, folding path, and output configurations by programming the loading sequence (compression or twist).

Such experimental capability opens up numerous applications for Kresling origami, particularly in the field of mechanical computing. One of the significant challenges in this research field is to achieve multiple mechanical logic networks, essentially determining the folding sequence of the origami assembly, within a single structure through the control of loading sequence (Yasuda et al., 2021).

CRediT authorship contribution statement

Shixi Zang: Writing – review & editing, Writing – original draft, Visualization, Validation, Methodology, Investigation, Formal analysis, Data curation. **Diego Misseroni:** Writing – review & editing, Writing – original draft, Visualization, Resources, Methodology, Investigation, Funding acquisition, Formal analysis, Conceptualization. **Tuo Zhao:** Writing – review & editing, Writing – original draft, Visualization, Validation, Methodology, Investigation, Formal analysis, Data curation, Conceptualization. **Glaucio H. Paulino:** Writing – review & editing, Writing – original draft, Supervision, Resources, Project administration, Methodology, Investigation, Funding acquisition, Conceptualization.

Declaration of competing interest

The authors declare that they have no known competing financial interests or personal relationships that could have appeared to influence the work reported in this paper.

Data availability

Data will be made available on request.

Acknowledgments

We acknowledge financial support from National Science Foundation project CMMI-2323276, and from the European Union project ERC-2022-COG-101086644-SFOAM.

Appendix A. Theoretical details

A.1. Initial configuration

As shown in Fig. 4A, the initial configuration in the deployed state is described by six geometrical parameters: three side lengths, a_0, b_0, c_0, and three dihedral angles δ_{a0}, δ_{b0}, δ_{c0}. Given four intrinsic parameters, r, n, h_0, θ_0, we can calculate the three side lengths as follows:

$$a_0 = 2r\sin(\pi/n) \tag{A.1}$$

$$b_0 = \sqrt{h_0^2 + p^2} = \sqrt{h_0^2 + 4r^2\sin^2(\theta_0/2)} \tag{A.2}$$

$$c_0 = \sqrt{h_0^2 + m^2} = \sqrt{h_0^2 + 4r^2\sin^2(\theta_0/2 + \pi/n)} \tag{A.3}$$

The dihedral angle δ_{a0}, as illustrated in the orange triangle in Fig. 4A and C, can be calculated by h_0 and q, i.e. $\tan\delta_{a0} = h_0/q$. Given $q = m\sin(\theta_0/2) = 2r\sin(\theta_0/2 + \pi/n)\sin(\theta_0/2)$, δ_{a0} can be obtained as:

$$\delta_{a0} = \arctan\frac{h_0}{2r\sin(\theta_0/2 + \pi/n)\sin(\theta_0/2)} \tag{A.4}$$

Using the pink and purple triangles in Fig. 4A and C, we calculate the two dihedral angles as $\delta_{b0} = \pi - \gamma$ and $\delta_{c0} = \pi - \beta$, where γ and β are derived from vectors $\vec{n}_1$, $\vec{n}_2$, and $\vec{n}_3$. In the Cartesian coordinate system $Oxyz$ (Fig. 4A), the three vectors are expressed as $\vec{n}_1 = \overrightarrow{A_1B_2} \times \overrightarrow{A_1A_2}$, $\vec{n}_2 = \overrightarrow{A_1B_1} \times \overrightarrow{A_1B_2}$, and $\vec{n}_3 = \overrightarrow{B_1B_2} \times \overrightarrow{B_1C_2}$. Then, the sector angle between the vectors can be obtained by $\cos\gamma = (\vec{n}_2 \cdot \vec{n}_3)/(\|\vec{n}_2\|\|\vec{n}_3\|)$ and $\cos\beta = (\vec{n}_1 \cdot \vec{n}_2)/(\|\vec{n}_1\|\|\vec{n}_2\|)$. Substituting the coordinates of vertices into these equations, we have:

$$\delta_{b0} = \pi - \arccos\frac{h_0^2\cos(\theta_0 + 2\pi/n) - r^2[\cos(\theta_0 + \pi/n) - \cos(\pi/n)]^2}{h_0^2 + r^2[\cos(\theta_0 + \pi/n) - \cos(\pi/n)]^2} \tag{A.5}$$

$$\delta_{c0} = \pi - \arccos\frac{h_0^2\cos\theta_0 - r^2[\cos(\theta_0 + \pi/n) - \cos(\pi/n)]^2}{h_0^2 + r^2[\cos(\theta_0 + \pi/n) - \cos(\pi/n)]^2} \tag{A.6}$$

A.2. Folding configuration

Similarly, we obtain expressions of the six geometric parameters in a folding configuration (Fig. 4B):

$$a = 2r\sin(\pi/n) \tag{A.7}$$

$$b(u,\varphi) = \sqrt{h^2 + 4r^2\sin^2(\theta/2)} \tag{A.8}$$

$$c(u,\varphi) = \sqrt{h^2 + 4r^2\sin^2(\theta/2 + \pi/n)} \tag{A.9}$$

$$\delta_a(u,\varphi) = \arctan\frac{h}{2r\sin(\theta/2 + \pi/n)\sin(\theta/2)} \tag{A.10}$$

$$\delta_b(u,\varphi) = \pi - \arccos\frac{h^2\cos(\theta + 2\pi/n) - r^2[\cos(\theta + \pi/n) - \cos(\pi/n)]^2}{h^2 + r^2[\cos(\theta + \pi/n) - \cos(\pi/n)]^2} \tag{A.11}$$

$$\delta_c(u,\varphi) = \pi - \arccos\frac{h^2\cos\theta - r^2[\cos(\theta + \pi/n) - \cos(\pi/n)]^2}{h^2 + r^2[\cos(\theta + \pi/n) - \cos(\pi/n)]^2} \tag{A.12}$$

Note that by substituting the relationship $h = h_0 - u$ and $\theta = \varphi + \theta_0$ (illustrated in Fig. 4) into Eqs. (A.7)–(A.12), we can obtain Eqs. (1)–(6) in Section 3.

A.3. Solutions to the analytical formulation

Here, we present a numerical solution scheme solving the theoretical formulations Eqs. (16)–(19) in Section 3.

Solving $\partial U/\partial\varphi = 0$ *and* $\partial U/\partial u = 0$. We define the accuracy of the numerical solution by the parameter n_v. The two variables (u and φ) can be described by two sets, S_u and S_φ, involving n_v members:

$$S_u = \{u_i\ (i = 1, 2, \dots, n_v) \mid 0 \le u_i \le (h_0 - h_{\text{folded}})\} \tag{A.13}$$

$$S_\varphi = \{\varphi_j\ (j = 1, 2, \dots, n_v) \mid 0 \le \varphi_j \le (\theta_{\max} - \theta_0)\} \tag{A.14}$$

By combining Eqs. (A.13) and (A.14), a new set with $n_v \times n_v$ members is expressed as:

$$S = \{(u_i, \varphi_j)\ (i, j = 1, 2, \dots, n_v) \mid 0 \le u_i \le (h_0 - h_{\text{folded}}),\ 0 \le \varphi_i \le (\theta_{\max} - \theta_0)\} \tag{A.15}$$

Next, we demonstrate the process of solving $\partial U/\partial\varphi = 0$ and $\partial U/\partial u = 0$ via an example considering $n_v = 5000$, $h_0 = 39.48$, $h_{\text{folded}} = 0$, $\theta_{\max} = 90°$, $\theta_0 = 30°$, $n = 6$, $r = 30$, $k_s = 50$ and $k_r = 5 \times 10^{-3}$. The solution scheme is summarized in four steps as follows:

Step 1: We substitute Eq. (A.15) into Eq. (9), and obtain an energy surface with $n_v \times n_v$ (5000 × 5000) nodes — see the gray surface in Fig. A.1.

Step 2: For $i = 1$, we assume $u_1 = 10 \in (0, 39.48)$, and define the set $S_{u_1} \in S$ as:

$$S_{u_1} = \{(u_1 = 10, \varphi_j)\ (j = 1, 2, \dots, 5000) \mid 0 \le \varphi_j \le 60\} \tag{A.16}$$

Substituting Eq. (A.16) into Eq. (9), we obtain an energy curve denoted by $U(u_1 = 10, \varphi)$ (see the dark blue solid line in Fig. A.1A).

Step 3: We find the minimum point on the energy curve $U(u_1 = 10, \varphi)$ and denote the point (i.e., the light blue dot in Fig. A.1A) as $(u_1 = 10, \varphi = 28.65)$, which satisfies the following condition:

$$\frac{\partial U(u_1 = 10, \varphi)}{\partial\varphi}\Big|_{\varphi=28.65} = 0 \tag{A.17}$$

Thus, $(u_1 = 10, \varphi = 28.65)$ is one solution of $\partial U/\partial\varphi = 0$.

Repeating Steps 2 and 3 for i varying from 2 to 5000, we obtain 5000 solutions of $\partial U/\partial\varphi = 0$ and denote them by the set S_{axial} as follows:

$$S_{\text{axial}} = \{(u_i, \varphi)\ (i = 1, 2, \dots, n_v) \mid 0 \le u_i \le 39.48,\ \frac{\partial U(u_i, \varphi)}{\partial\varphi} = 0\} \tag{A.18}$$

The solution set S_{axial} corresponds to the relationship $\varphi = f_F(u)$ presented in Section 3. Substituting Eq. (A.18) into Eq. (9), we obtain the elastic energy of the Kresling cell under axial loading (i.e., the light blue solid line in Fig. A.1B).

Step 4: For $j = 1$, we assume $\varphi_1 = 20 \in (0, 60)$, and define the set $S_{\varphi_1} \in S$ as:

$$S_{\varphi_1} = \{(u_i, \varphi_1 = 20)\ (i = 1, 2, \dots, 5000) \mid 0 \le u_i \le 39.48\} \tag{A.19}$$

Substituting Eq. (A.19) into Eq. (9), we obtain an energy curve denoted by $U(u, \varphi_1 = 20)$ (see the purple dashed line in Fig. A.1C).

Step 5: We find the minimum point on the energy curve $U(u, \varphi_1 = 20)$ and denote the point (i.e., the orange dot in Fig. A.1C) as $(u = 6.33, \varphi_1 = 20)$, which satisfies the following condition:

$$\frac{\partial U(u, \varphi_1 = 20)}{\partial u}\Big|_{u=6.33} = 0 \tag{A.20}$$

Thus, $(u = 6.33, \varphi_1 = 20)$ is one solution of $\partial U/\partial u = 0$.

Repeating Steps 4 and 5 for j changing from 2 to 5000, we obtain 5000 solutions of $\partial U/\partial u = 0$ and denote them by the set $S_{\text{torsional}}$ as follows:

$$S_{\text{torsional}} = \{(u, \varphi_j)\ (j = 1, 2, \dots, n_v) \mid 0 \le \varphi_j \le 60,\ \frac{\partial U(u, \varphi_j)}{\partial u} = 0\} \tag{A.21}$$

The solution set $S_{\text{torsional}}$ corresponds to the relationship $u = f_T(\varphi)$ presented in Section 3. Substituting Eq. (A.21) into Eq. (9), we obtain the elastic energy of the Kresling cell under torsional loading (i.e., the orange dash line in Fig. A.1D).

Solving stable states, Eqs. (17) and (19) . As shown in Section 3.3, the solutions of stable states satisfy the following conditions:

$$\begin{aligned}&\partial U/\partial u = 0,\ \ \partial U/\partial\varphi = 0,\\ &\partial^2 U/\partial u^2 > 0 \text{ (for axial loading) and } \partial^2 U/\partial\varphi^2 > 0 \text{ (for torsional loading)}\end{aligned} \tag{A.22}$$

The two conditions, $\partial U/\partial\varphi = 0$ and $\partial U/\partial u = 0$, indicate that the solutions of Eq. (A.22) are $S_{\text{axial}} \cap S_{\text{torsional}}$. For a cell with two stable states, the intersection of the two solution sets is as follows:

$$S_{\text{axial}} \cap S_{\text{torsional}} = \{(0, 0), (12.1, 33), (27.7, 55)\} \tag{A.23}$$

Since $(12.1, 33)$ violates the second order conditions in Eq. (A.22), the solution set is $\{(0, 0), (27.7, 55)\}$. The 2nd stable point $(27.7, 55)$ is illustrated by the black dot in Fig. A.1E.

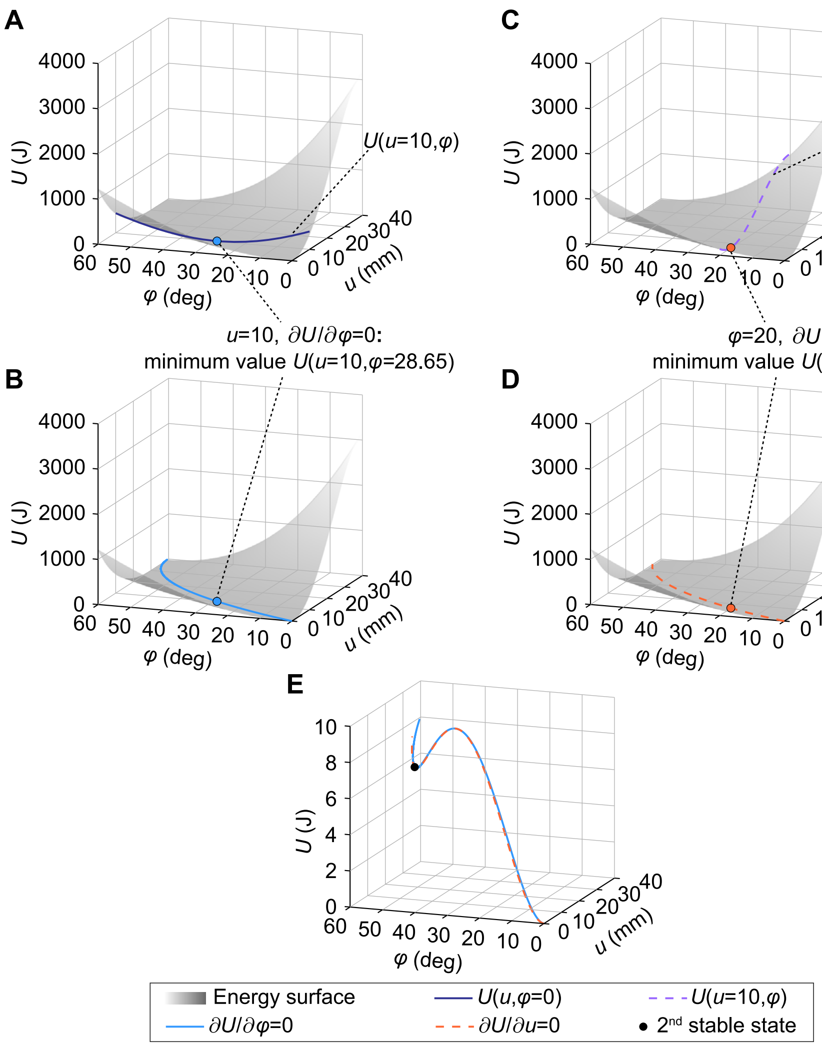

Fig. A.1. Illustration of solving the analytical formulation of the Kresling cell. (A) Energy surface, curve $U(u = 10, \varphi)$, and minimum value $U(u = 10, \varphi = 28.65)$. (B) Energy surface, curve $\partial U/\partial \varphi = 0$, and point $U(u = 10, \varphi = 28.65)$. (C) Energy surface, curve $U(u, \varphi = 20)$, and minimum value $U(u = 6.33, \varphi = 20)$. (D) Energy surface, curve $\partial U/\partial u = 0$, and point $U(u = 6.33, \varphi = 20)$. (E) Energy curves $\partial U/\partial \varphi = 0$ and $\partial U/\partial u = 0$, and 2nd stable state. In this figure, we select $n = 6$, $r = 30$, $\theta_0 = 30°$, $k_s = 50$ and $k_r = 5 \times 10^{-3}$.

Appendix B. Details of specimen fabrication

The experimental specimens are made of a composite material consisting of two layers of paper and one layer of tape. Before joining the three layers, we utilized a laser cutter to remove the top and bottom layers of paper from the composite material at crease areas (see the black lines in Fig. B.1). Then, the two layers of paper were attached to the two sides of the 0.17 mm-thick 3M 9474LE adhesive transfer tape. As shown in Fig. B.1, all three layers of the composite material were cut at mountain crease areas. Finally, the patterned composite material was assembled to the folded configuration of the Kresling cell, where the top and bottom polygons were glued to a thin 3D-printed plate with magnets, respectively.

Appendix C. Effect of loading rates

To explain the effect of loading rate on the experimental results, we have conducted compression tests under 1.5 mm/s, 0.25 mm/s, and 0.05 mm/s; and torsional tests under 2.5 deg/s, 0.5 deg/s, and 0.1 deg/s. The experimental results reveal that our novel experimental fixtures are slightly affected by the loading rate. The difference observed at the initial peak point of the force/torque curve (Fig. C.1A and C) is caused by the viscoelasticity of the 3M tape used in the composite material of our experiment specimens. Since there is no obvious trend or pattern observed in the curves (Fig. C.1B and D) while increasing the loading rate, we conclude that loading rates do not influence the torque measurement during the compression test, and the force measurement under the torsional test, respectively. Those observations justify the efficiency of our setups in terms of torque/force decoupling.

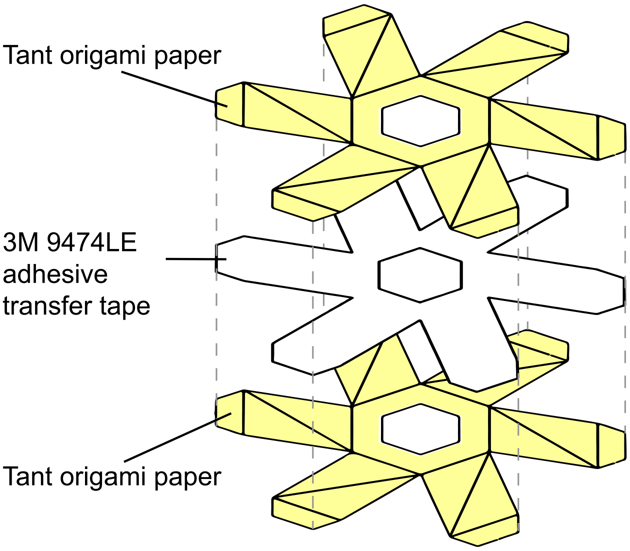

Fig. B.1. Details of fabricating composite Kresling cell.

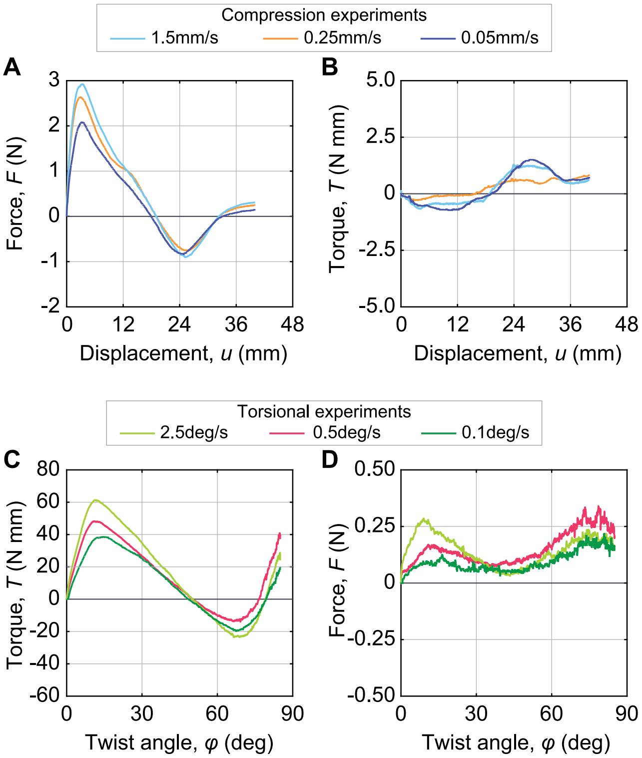

Fig. C.1. Experimental results under different loading rates. (A) Force and (B) torque measurements of compression experiments under 1.5 mm/s, 0.25 mm/s, and 0.05 mm/s. (C) Torque and (D) force measurements of torsional experiments under 2.5 deg/s, 0.5 deg/s, and 0.1 deg/s.

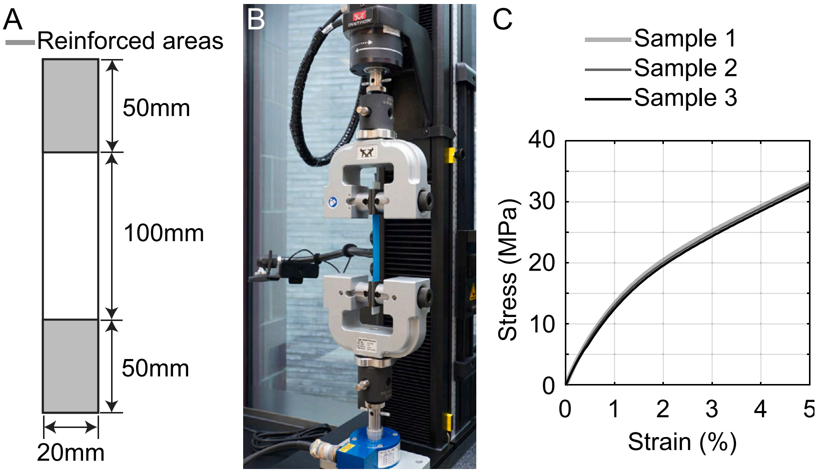

Fig. D.1. Tensile experiment of the composite material. (A) Experimental specimens. (B) A photograph of the setup. (C) Stress vs. strain curves.

Table D.1
Rotational stiffness results.

Sample	k_r (N mm (rad mm)$^{-1}$)	R^2
1	0.0057	0.9124
2	0.0050	0.9311
3	0.0054	0.9364
Average	0.0054	0.9266

Appendix D. Material and rotational stiffness experiments

D.1. Material experiment

In the material experiment, we use the rectangular specimen (Liu et al., 2020) (dimensions are shown in Fig. D.1A) with the same thickness and fabrication method as the composite material in Appendix B. The two reinforced areas on the specimen in Fig. D.1A are connected to the tensile fixtures of the Instron loading frame machine in Fig. D.1B. We tested three samples and drew the experimental results in Fig. D.1C. The elastic modulus, E, used in this paper is the secant modulus at 0.5% strain in Fig. D.1C, where $E = 1503.27$ MPa.

D.2. Rotational stiffness experiment

To obtain the crease rotational stiffness, we design the experimental specimen shown in Fig. D.2A. The primary crease, indicated by the middle blue line, is fabricated in the same way as the creases in Appendix B, while the weaker creases, indicated by dot lines, are made of a softer tape than the 3M 9474LE adhesive transfer tape (used for the primary crease). In order to estimate the rotational stiffness of the primary crease, we repeatedly pre-folded the weaker creases about 10 times to make them nearly rotation-free. From the schematic in Fig. D.2B and C, we calculate the moment and rotation angle of the primary crease as follows:

$$M = FL + G_\mathrm{p}L/2 \tag{D.1}$$

$$\omega = 2[\arcsin(d_0/2a) - \arcsin(d/2a)] \tag{D.2}$$

where $L = \sqrt{a^2 - (d/2)^2}$. According to Fig. D.2D, we can calculate the rotational stiffness per unit length, k_r, by linear regression.

$$k_r = \Delta M/(L_\mathrm{s}\Delta\omega) \tag{D.3}$$

The results of rotational stiffness are shown in Table D.1. The term R^2 denotes the coefficient of determination for the linear regression model.

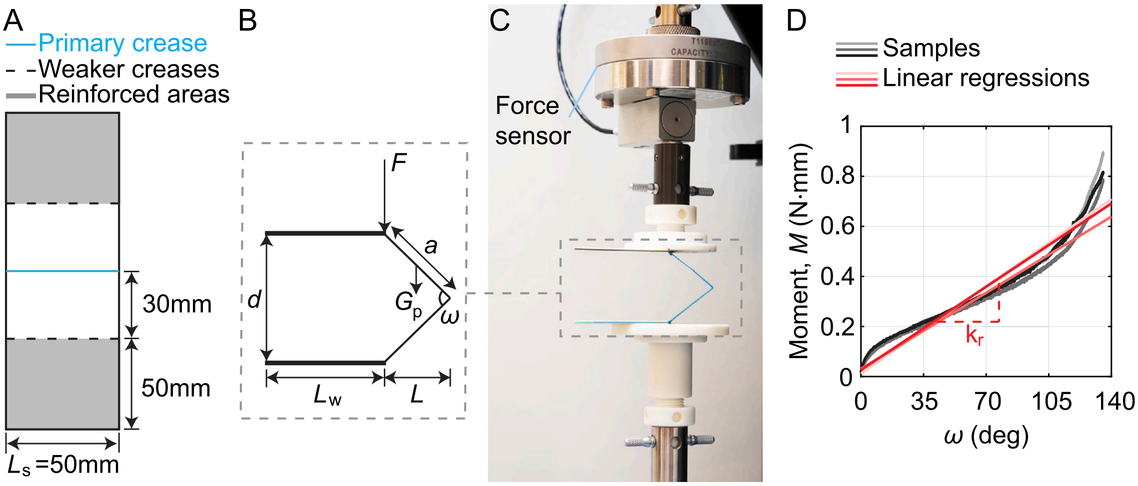

Fig. D.2. Crease rotational stiffness experiment. (A) Design of experimental specimens. The primary crease is fabricated using the same way as the creases in Kresling sample. The weaker creases are fabricated by tape softer than the primary crease and pre-folded 10 times. (B) Schematic and (C) a photograph of the setup. (D) Experimental results and rotational stiffness, k_r, obtained by linear regression.

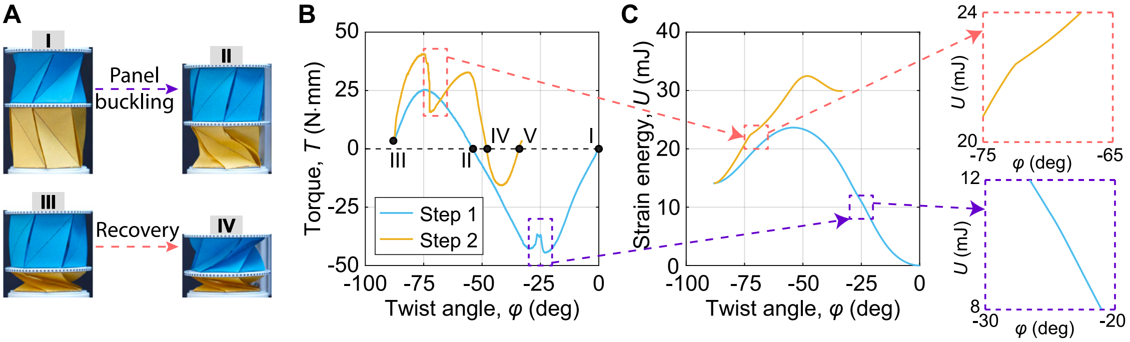

Fig. E.1. Buckling effect on the energy landscape. (A) Photos of configurations I, II, III, and IV show the panel buckling of the $\varphi_{\max} = 60°$ cell. (B) Experimental results of 2-cell Kresling array with opposite chirality under torsional (free-translation) loading condition (Fig. 12C). (C) Left: Energy curve obtained from the data in (A). Right: Details of the energy curve corresponding to the two drops in (A).

Appendix E. Two-cell Kresling array

E.1. Instability/buckling issue

We investigate the buckling effect observed in the torsional experiments of the 2-cell array with opposite chirality. The panels of the $\varphi_{\max} = 60°$ cell (blue color) buckled during the folding process from configuration I to configuration II ($\varphi \approx -25°$), and “recovered” during the folding process from configuration III to configuration IV ($\varphi \approx -73°$), as shown in Fig. E.1A. This leads to local oscillations in Fig. E.1B resulting in varying slopes of the energy curve in Fig. E.1C.

E.2. Simplified theoretical analysis

We present an extended theoretical analysis for 2-cell Kresling arrays. The analysis, inspired by Lu et al. (2022), combines single cell solutions (e.g., $\varphi_{\max} = 60°$ cell and $\varphi_{\max} = 90°$ cell) in two steps as follows: **(1)** The $\varphi_{\max} = 60°$ cell in the array folds and the corresponding theoretical result is taken as the single cell solution; **(2)** We assume that the $\varphi_{\max} = 60°$ cell remains in the folded configuration, and the $\varphi_{\max} = 90°$ cell starts to fold. The corresponding deformation (displacement/twist angle) begins at the endpoint of step (1). The corresponding force/torque obtained in step (2) is a superposition of two single cell solutions. Fig. E.2 compares the theoretical solutions and corresponding experimental results for the 2-cell arrays with different arrangements of chirality under various loading conditions. Since we do not consider buckling in the analytical formulation, we expect discrepancies between theoretical and experimental results. Besides the buckling effects, other factors might contribute to those discrepancies, such as the nature of the simplified theoretical modeling, and not accounting for the self-weight of the cells.

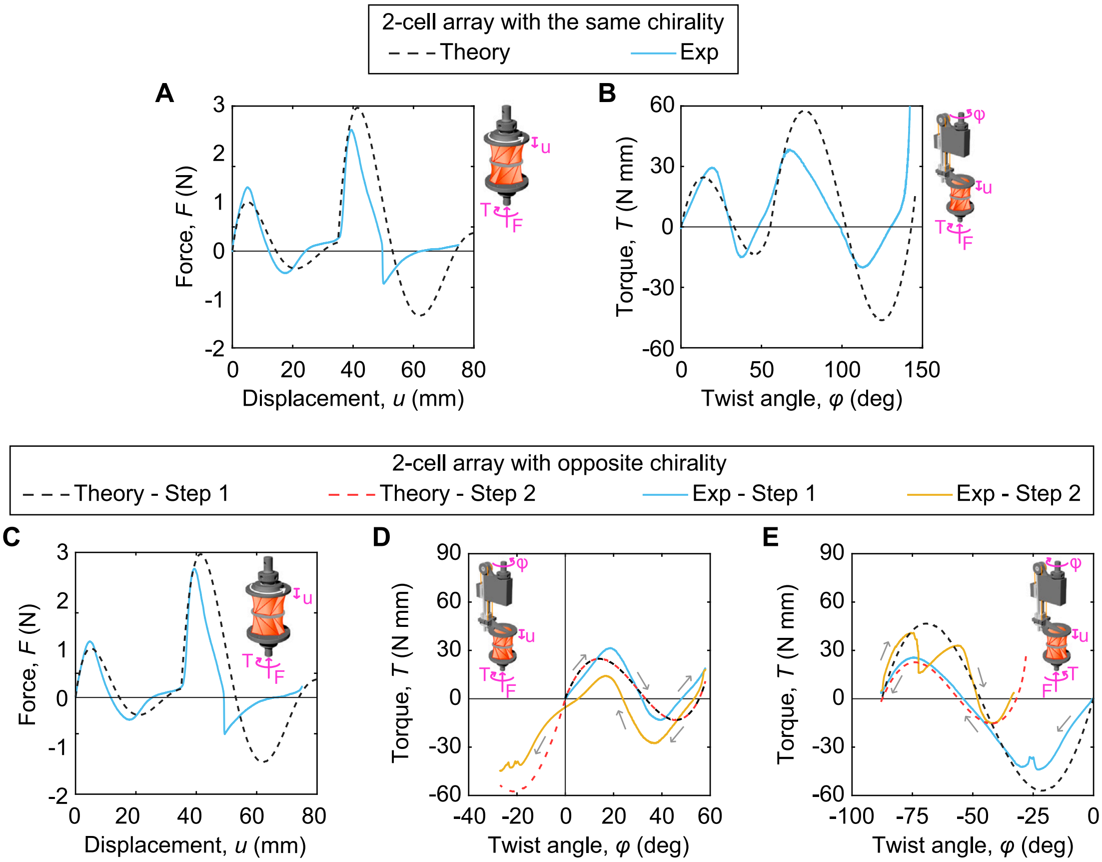

Fig. E.2. Comparison between theoretical and experimental results of 2-cell arrays. The theoretical results are the combination of the theory of two unit cells. (A) Compression and (B) torsional experiments on the 2-cell array with the same chirality. (C) Compression experiment, (D) torsional experiment starting from controlling $\varphi_{\max} = 60°$ cell, and (E) torsional experiment starting from controlling $\varphi_{\max} = 90°$ cell on the 2-cell array with opposite chirality. Grey arrows show the direction of loading.

Appendix F. Nomenclature

Geometric parameters of Kresling origami cell

δ_{a0}	Initial dihedral angle between surface polygons and side triangular panels
δ_a	Dihedral angle between surface polygons and side triangular panels
δ_{b0}	Initial dihedral angle between side triangular panels along mountain folds
δ_b	Dihedral angle between side triangular panels along mountain folds
δ_{c0}	Initial dihedral angle between side triangular panels along valley folds
δ_c	Dihedral angle between side triangular panels along valley folds
θ	Relative angle between the top and bottom polygons
θ_0	Relative angle between the top and bottom polygons in the deployed state
$\theta_{\max}$	Relative angle between the top and bottom polygons in the folded configuration
φ	Twisting angle of the top polygon with bottom polygon fixed
$\varphi_{\max}$	Maximum value of φ, i.e., $\theta_{\max} - \theta_0$
A	Cross-section area of the bar element
a	Side length of polygons
a_0	Initial side length of polygons
A_b	Cross-section area of the bar element of mountain creases
A_c	Cross-section area of the bar element of valley creases
b	Length of mountain creases
b_0	Initial length of mountain creases
c	Length of valley creases
c_0	Initial length of valley creases

h	Height of Kresling origami cell
h_0	Height in the initial configuration
h_{folded}	Height in the folded configuration
n	Number of edges of the top/bottom polygon
n_a	Number of edges of top and bottom surfaces
n_b	Number of mountain creases
n_c	Number of valley creases
r	The radius of the circumscribed circle of polygon
t	Thickness of the composite material used in experimental specimen
u	Distance between points B_2 and B_2' in the z-direction

Mechanical parameters of Kresling origami cell

Π	Total potential energy
E	Elastic modulus
e_1	Component of δ_b and δ_c items in force and torque equations
e_1'	Derivation of e_1
F	Axial force
$f_F(u)$	Relationship between φ and u derived from $\partial U/\partial\varphi = 0$
$f_T(\varphi)$	Relationship between u and φ derived from $\partial U/\partial u = 0$
g_b	Component of the δ_b item in torque equation
g_c	Component of the δ_c item in torque equation
k_r	Rotational stiffness of the crease per unit length
k_s	Stretching stiffness of the material
$k_{r,a}$	Folding stiffness between surface polygons and side triangular panels
$k_{r,b}$	Folding stiffness between side triangular panels along mountain folds
$k_{r,c}$	Folding stiffness between side triangular panels along valley folds
$k_{s,b}$	Stretching stiffness of mountain creases
$k_{s,c}$	Stretching stiffness of valley creases
T	Torque
U	Total elastic energy
U_{bar}	Elastic energy stored in bar elements
U_{rot}	Elastic energy provided by rotational springs
W	Work

Parameters in appendix of theoretical details

β	Sector angle between vectors $\vec{n}_1$ and $\vec{n}_2$
γ	Sector angle between vectors $\vec{n}_2$ and $\vec{n}_3$
φ_j	The member in set S_φ
$\vec{n}_1$	Normal vector of the triangular panel $\triangle A_2A_1B_2$
$\vec{n}_2$	Normal vector of the triangular panel $\triangle A_1B_1B_2$
$\vec{n}_3$	Normal vector of the triangular panel $\triangle B_2B_1C_2$
m	Distance between points A_1 and S (the projection of point B_2 onto the bottom polygon)
n_v	Resolution of the scheme in the solution of the analytical formulation
p	Distance between points B_1 and S (the projection of point B_2 onto the bottom polygon)
q	Distance between points T (the projection of point B_2 onto the line A_1B_1) and S
S	Set of (u, φ)
S_{axial}	Solution set of the condition $\partial U/\partial\varphi = 0$
$S_{\text{tortional}}$	Solution set of the condition $\partial U/\partial u = 0$
S_φ	Set of variables φ
S_u	Set of variables u
S_{φ_1}	Set of $(u, \varphi = 20)$
S_{u_1}	Set of $(u = 10, \varphi)$
u_i	The member in set S_u

Parameters in appendix of stiffness experimental details

ω	Folding angle between two rectangular panels along primary crease
d	Distance between two weaker creases in the schematic of experimental setup
d_0	Initial distance between two weaker creases in the schematic of experimental setup
G_p	Gravity of one rectangular panel of the specimen in the schematic of experimental setup
L	Horizontal distance between the primary crease and the loading point
L_s	Length of the primary crease
L_w	Length of the reinforced area in the schematic of experimental setup
M	Moment of the primary crease
v	Poisson's ratio

Appendix G. Supplementary data

Supplementary material related to this article can be found online at https://doi.org/10.1016/j.jmps.2024.105630.

References

Bhovad, P., Kaufmann, J., Li, S., 2019. Peristaltic locomotion without digital controllers: Exploiting multi-stability in origami to coordinate robotic motion. Extreme Mech. Lett. 32, 100552.

Cai, J., Deng, X., Zhou, Y., Feng, J., Tu, Y., 2015. Bistable Behavior of the Cylindrical Origami Structure With Kresling Pattern. J. Mech. Des. 137 (6), 061406.

Cleveland, J.M., Zhang, Y., Restrepo, D., Mankame, N.D., Zavattieri, P.D., 2016. Mechanical investigation of phase-transforming cellular and Origami materials. In: The Summer Undergraduate Research Fellowship (SURF) Symposium.

Huang, C., Tan, T., Hu, X., Yang, F., Yan, Z., 2022a. Bio-inspired programmable multi-stable origami. Appl. Phys. Lett. 121 (5), 051902.

Huang, C., Tan, T., Wang, Z., Nie, X., Zhang, S., Yang, F., Lin, Z., Wang, B., Yan, Z., 2022b. Bistable programmable origami based soft electricity generator with inter-well modulation. Nano Energy 103, 107775.

Jin, T., Li, L., Wang, T., Wang, G., Cai, J., Tian, Y., Zhang, Q., 2022. Origami-inspired soft actuators for stimulus perception and Crawling Robot applications. IEEE Trans. Robot. 38 (2), 748–764.

Jules, T., Reid, A., Daniels, K.E., Mungan, M., Lechenault, F., 2022. Delicate memory structure of origami switches. Phys. Rev. Res. 4 (1), 013128.

Kresling, B., 2008. Natural twist buckling in shells: from the hawkmoth’s bellows to the deployable Kresling-pattern and cylindrical Miura-ori. In: Proceedings of the 6th International Conference on Computation of Shell and Spatial Structures IASS-IACM 2008: "Spanning Nano to Mega". https://hdl.handle.net/1813/11530.

Lang, R.J., 2017. Twists, Tilings, and Tessellations: Mathematical Methods for Geometric Origami. CRC Press.

Li, Z., Kidambi, N., Wang, L., Wang, K.-W., 2020. Uncovering rotational multifunctionalities of coupled kresling modular structures. Extreme Mech. Lett. 39, 100795.

Liu, K., Novelino, L.S., Gardoni, P., Paulino, G.H., 2020. Big influence of small random imperfections in origami-based metamaterials. Proc. R. Soc. Lond. Ser. A Math. Phys. Eng. Sci. 476 (2241), 20200236.

Liu, K., Paulino, G., 2017. Nonlinear mechanics of non-rigid origami: an efficient computational approach. Proc. R. Soc. A 473 (2206), 20170348.

Lu, L., Dang, X., Feng, F., Lv, P., Duan, H., 2022. Conical Kresling origami and its applications to curvature and energy programming. Proc. R. Soc. A 478 (2257), 20210712.

Masana, R., Daqaq, M.F., 2019. Equilibria and bifurcations of a foldable paper-based spring inspired by Kresling-pattern origami. Phys. Rev. E 100 (6), 063001.

Masana, R., Khazaaleh, S., Alhussein, H., Crespo, R.S., Daqaq, M.F., 2020. An origami-inspired dynamically actuated binary switch. Appl. Phys. Lett. 117 (8), 081901.

Nayakanti, N., Tawfick, S.H., Hart, A.J., 2018. Twist-coupled kirigami cells and mechanisms. Extreme Mech. Lett. 21, 17–24.

Pagano, A., Leung, B., Chien, B., Yan, T., Wissa, A., Tawfick, S., 2016. Multi-stable origami structure for crawling locomotion. In: Smart Materials, Adaptive Structures and Intelligent Systems, vol. 50497, American Society of Mechanical Engineers, V002T06A005.

Pagano, A., Yan, T., Chien, B., Wissa, A., Tawfick, S., 2017. A crawling robot driven by multi-stable origami. Smart Mater. Struct. 26 (9), 094007.

Wilson, L., Pellegrino, S., Danner, R., 2013. Origami sunshield concepts for space telescopes. In: 54th AIAA/ASME/ASCE/AHS/ASC Structures, Structural Dynamics, and Materials Conference. p. 1594.

Yang, H., Lu, H., Shu, D.-W., Fu, Y.Q., 2023. Multimodal origami shape memory metamaterials undergoing compression-twist coupling. Smart Mater. Struct..

Yasuda, H., Buskohl, P.R., Gillman, A., Murphey, T.D., Stepney, S., Vaia, R.A., Raney, J.R., 2021. Mechanical computing. Nature 598 (7879), 39–48.

Yasuda, H., Miyazawa, Y., Charalampidis, E.G., Chong, C., Kevrekidis, P.G., Yang, J., 2019. Origami-based impact mitigation via rarefaction solitary wave creation. Sci. Adv. 5 (5), eaau2835.

Yasuda, H., Tachi, T., Lee, M., Yang, J., 2017. Origami-based tunable truss structures for non-volatile mechanical memory operation. Nat. Commun. 8 (1), 1–7.

Zhang, Q., Wang, X., Cai, J., Feng, J., 2021b. Motion paths and mechanical behavior of origami-inspired tunable structures. Mater. Today Commun. 26, 101872.

Zhang, M., Yang, J., Zhu, R., 2021a. Origami-Based Bistable Metastructures for Low-Frequency Vibration Control. J. Appl. Mech. 88 (5), 051009.